Available online at www.sciencedirect.com
ScienceDirect
Journal of Computational Physics 224 (2007) 489–518
JOURNAL OF COMPUTATIONAL PHYSICS
www.elsevier.com/locate/jcp

Finite element/volume solution to axisymmetric conservation laws

A. Guardone *, L. Vigevano

Dipartimento di Ingegneria Aerospaziale, Politecnico di Milano, Via La Masa 34, 20158 Milano, Italy

Received 29 December 2005; received in revised form 11 July 2006; accepted 25 August 2006
Available online 16 October 2006

Abstract

Conservation laws in axisymmetric geometries are discretized for the first time according to the node-pair framework of Selmin [Comput. Methods Appl. Mech. Eng. 102 (1993) 107–138]. A relation is found linking the node-pair finite element discretization to the finite volume scheme, opening the way to the use of standard finite volume stabilization techniques and high-resolution schemes in the computation of axisymmetric problems. By construction, the treatment of the axis is naturally built-in inside the basic structural elements of the spatial discretization. Numerical results are presented and compared to the exact solution for scalar advection in a source flow, considering both continuous and discontinuous initial profiles. Numerical simulations of compressible flows include the complex dynamical interaction and propagation of waves in a shock-tube experiment and the steady flow at the exit of under-expanded and sonic nozzles. Numerical results are found to agree fairly well with experimental data, demonstrating the validity of the proposed approach.

Keywords: Conservation laws; Scalar advection; Euler equations; Axisymmetric flows; Unstructured grids; Hybrid finite element/volume schemes; High-resolution TVD schemes

1. Introduction

The close connection between the finite element (FE) Galerkin and finite volume (FV) discretizations for conservation laws on unstructured meshes has been pointed out by several authors at the beginning of the '90s, see, e.g. [1–3]. This clarification led to the development of several hybrid FV/FE methods in two- and three-dimensions, suited for unstructured or hybrid meshes and edge-based data structures [4–6]. The typical approach to build one of such methods has been to evaluate the fluxes of the Euler equations by a classical node-centered FV scheme and to exploit the FE viewpoint to discretize the viscous or diffusion terms of the Navier–Stokes equations as well as to possibly estimate the solution gradients, needed by high order reconstruction schemes [7]. In the

* Corresponding author. Tel.: +39 02 23998393; fax: +39 02 39338334.
E-mail address: guardone@aero.polimi.it (A. Guardone).

0021-9991/$ - see front matter © 2006 Elsevier Inc. All rights reserved.
doi:10.1016/j.jcp.2006.08.018

above approach, according to the FV methodology, metric quantities emerge from the geometric characteristics of the mesh.

A different approach was proposed by Selmin [3] for inviscid flows and subsequently extended to viscous flows by Selmin and Formaggia [8]. The Bubnov–Galerkin weak formulation of the governing equations is considered in this case and the so-called group representation of the fluxes is then introduced to simplify the evaluation of the FE integrals. FV metrics quantities are eventually defined entirely upon FE integrals of the shape functions so that an equivalent FE/FV discretization is obtained for both the convective and diffusive terms. The advantage of this approach is that it is not limited to linear finite elements and may be generalized to Lagrangian elements of any order, although a direct connection with the FV discretization on the median-based dual control volume is limited to linear and approximations. Thanks to the common FE/FV representation of the discrete equations, standard FV stabilization techniques, such as the Jameson–Schmidt–Turkel artificial viscosity scheme [9], the flux vector splitting upwind scheme of Van Leer [10] or the flux difference upwind scheme of Roe [11], became readily available within the FE method for advection dominated problems. Eventually, these techniques were combined with higher-order schemes according to the total variation diminishing (TVD) approach [12].

The pivotal idea in the determination of the FV/FE equivalence is the introduction of a *node-pair* data structure. In FV approximations, a node-pair is a couple of grid nodes which share a common FV interface. Under the Lagrangian FE point of view, a node-pair is a couple of nodes whose associated shape function supports overlap. The companion idea of defining suitable metric quantities on each node-pair or node of the triangulation, a metric quantity being either the results of a FE integral or a geometrical entity associated with a given FV, allowed for the development of very efficient computer algorithms, since the metric quantities can be computed once and for all at the beginning of the computation. No FE quadrature is therefore required as the computation progresses.

The FE/FV node-pair approach to the equations describing axially symmetric conservation laws formulated in a cylindrical coordinate system is developed in the present paper. The equivalence between FE and FV – established in [3,8] for the equations written in Cartesian coordinates – is extended here to the axisymmetric case, although, even for the simplest situation of linear elements, it is not possible to define the shape of the corresponding control volume. Nevertheless, this does not prevent to draw advantage of the underlying connection in order to employ upwind corrections to the convective fluxes. The correct treatment of the discrete equations at the axis of symmetry is naturally built in the method, by construction of the FE/FV metric quantities. This is not the case for other types of discretizations that locate the mesh nodes on the symmetry axis, as for instance finite differences or standard node-centered or cell-vertex FV. The imposition of point-wise boundary conditions on the axis in these methods is complicated by the singularity of the cylindrical coordinates and it requires either to approximate the singular terms with ad hoc procedures (e.g. L'Hopital rule) [13,14] or to resort to complex geometrical calculations of the control volume centroids [15].

The presentation of the method and of the numerical results is as follows. The node-pair FE and FV schemes are presented for a scalar conservation law and the equivalence between the FV and the FE approaches is demonstrated in Section 2. In Section 3, the Euler equations for axially symmetric compressible flows are briefly recalled and the the node-pair representations of the FE and FV schemes for the Euler equation are given. A hybrid finite element/volume high-resolution TVD scheme is derived and the discretization of the time derivative for calculating unsteady and steady solutions is discussed in Section 4. The standard high-resolution procedure is modified to account also for high-order FE contributions, which were neglected in [3,8] because they have no FV counterparts, namely, they are not present in a standard FV scheme. The computation of the source term for the Euler equations for axisymmetric flows – including a possibly non-zero tangential velocity (swirling flows) – is also detailed. In Section 5, the proposed scheme is applied to the computation of axially symmetric scalar advection problems and inviscid compressible flows. Results include the propagation of a shock wave from a partially-opened shock-tube diaphragm and the flow at the exit of under-expanded nozzles. Numerical results are compared to experimental data and discussed. A summary of the proposed scheme and final remarks are given in Section 6. Appendices A and B detail the derivation of the discrete equations and the extension of the scheme to swirling flows.

2. Scalar conservation law

The node-pair finite element/volume discretization of a scalar conservation law with axisymmetric solutions is now presented. The finite element representation of the conservation law is first described, where the flux function is approximated by means of a reinterpolation based on the same shape functions used to represent the unknown variable. Then, the node-pair formulation of the spatially discrete equations is derived. The finite volume discretization is also presented and the relation between finite volume and finite element approximations is discussed.

2.1. Governing equation

Let us consider the scalar conservation law in three spatial dimensions

$$\frac{\partial u}{\partial t} + \nabla \cdot \boldsymbol{f}(u) = 0, \tag{1}$$

where $u \in \mathbb{R}$, $u = u(\boldsymbol{x}, t)$ is the unknown with associated flux vector $\boldsymbol{f} \in \mathbb{R}^3$ and $\nabla \cdot \boldsymbol{f} = \frac{\partial f_x}{\partial x} + \frac{1}{y}\frac{\partial [y f_y]}{\partial y} + \frac{1}{y}\frac{\partial f_\theta}{\partial \theta}$, where x, y and θ are the axial, radial and angular coordinates in a cylindrical coordinate system, respectively, and f_x, f_y and f_θ are the corresponding components of the flux vector $\boldsymbol{f}$. The distance from the axis is denoted by letter y instead of the more usual symbols R or r, in order to have a notation encompassing both the axisymmetric cylindrical situation and the plane Cartesian one simply by introducing an integer switch parameter, see below. The solution u is sought for all $\boldsymbol{x} \in \Omega^{3D} \subset \mathbb{R}^3$, where Ω^{3D} is a three-dimensional axisymmetric region (see Fig. 1, left) and $t \in [0 : T] \subset \mathbb{R}^+$. For the above partial differential equation to be solvable, initial conditions at time $t = 0$ and suitable boundary conditions on the boundary $\partial\Omega^{3D}$ of Ω^{3D} are to be provided; for a detailed discussion, the interest reader is referred to the monograph of Godlewski and Raviart [16].

For axially symmetric problems u is independent from the angular coordinate θ and Eq. (1) reduces to

$$\frac{\partial u}{\partial t} + \frac{\partial f_x(u)}{\partial x} + \frac{1}{y}\frac{\partial [y f_y(u)]}{\partial y} = 0, \tag{2}$$

where f_x and f_y are the axial and radial components of $\boldsymbol{f}$, which is now a vector in $\mathbb{R}^2$. The solution $u(\boldsymbol{x}, t)$ to (2), with $\boldsymbol{x} \in \mathbb{R}^2$, is now sought for all $\boldsymbol{x} \in \Omega \subset \mathbb{R}^2$ and $t \in [0 : T] \subset \mathbb{R}^+$, where Ω is a two-dimensional open domain of an axial half plane $y > 0$. Note that the boundary $\partial\Omega$ of Ω may possibly have a (rectilinear) portion $\partial\Omega_{\text{axis}}$ lying on the axis x (see Fig. 1, right). The multiplication of this equation by y yields

$$\frac{\partial (yu)}{\partial t} + \nabla \cdot [y\boldsymbol{f}(u)] = 0, \tag{3}$$

where $\nabla \cdot \boldsymbol{q} = \frac{\partial q_x}{\partial x} + \frac{\partial q_y}{\partial y}$ is the standard two-dimensional divergence of a vector $\boldsymbol{q} = (q_x, q_y)^{\mathrm{T}} \in \mathbb{R}^2$ for the Cartesian coordinates (x, y) of the axial plane. This form of the equation is the key for building the solver for axially symmetric problems straightforwardly upon an existing 2D Cartesian solver for plane problems.

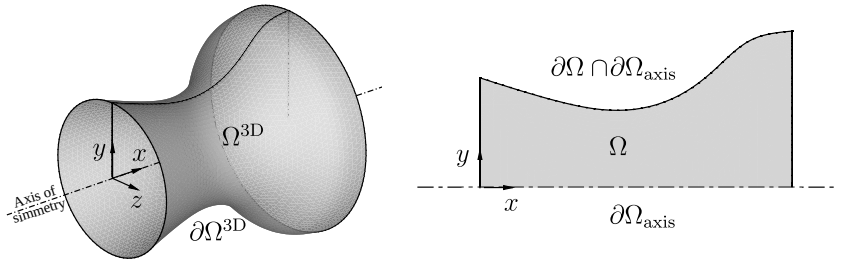

Fig. 1. Axisymmetric nozzle-like 3D geometry and definition of its section in an axial plane, with the 2D domain Ω and its boundary $\partial\Omega$. The continuous line indicates the partition $\partial\Omega \backslash \partial\Omega_{\text{axis}}$ of the boundary, with $\partial\Omega_{\text{axis}}$ portion of the domain (if any) belonging to the axis of symmetry.

The same form has been considered by Wood and Kleb in the development of a FV fluctuation splitting method for axisymmetric compressible flows [15]. It is also worth recalling that a different approach, termed the domain perturbation, has been followed by Goudjo and Desideri in which the scheme is derived as the limiting case of a three-dimensional FV discretization for a control volume of vanishing thickness [17].

Note that by switching to a cylindrical coordinate system a singularity at $y = 0$, namely, the axis of symmetry, has been introduced (cf. Eq. (2)). The singularity, which is not present in the model equation (1), was then apparently removed in (3). It is therefore necessary to investigate the behavior of Eq. (3) for $y \to 0$. From (3), one has

$$y\frac{\partial u}{\partial t} + y\nabla \cdot \boldsymbol{f}(u) + \boldsymbol{f}(u) \cdot \hat{\boldsymbol{y}} = 0,$$

where $\hat{\boldsymbol{y}}$ and is the unit vector normal to the x axis. Therefore,

$$\boldsymbol{f}(u) \cdot \hat{\boldsymbol{y}} \to 0 \quad \text{as } y \to 0, \tag{4}$$

that is, Eq. (3) is identically satisfied at the axis of symmetry provided that the flux component normal to the axis vanishes. Such a property of the governing equation is expected to be found also in its discretized counterpart.

2.2. Finite element discretization

The scalar conservation law (3) is now written in a weak or variational form according to the classical finite element method, see, e.g. [18]. The differential equation is first multiplied by test functions ϕ_h of Lagrangian type belonging to a suitable finite dimensional space $V_h \subset H^1(\Omega)$ and then integrated over the support Ω_i of each test function $\phi_i \in V_h$ to obtain

$$\int_{\Omega_i} y\phi_i \frac{\partial u}{\partial t} + \int_{\Omega_i} \phi_i \nabla \cdot [y\boldsymbol{f}(u)] = 0 \quad \forall i \in \mathscr{K},$$

where the symbol $\mathscr{K}$ denotes the set of all nodes of the triangulation. An integration by parts gives

$$\int_{\Omega_i} y\phi_i \frac{\partial u}{\partial t} - \int_{\Omega_i} y\boldsymbol{f}(u) \cdot \nabla\phi_i + \int_{\partial\Omega_i^\partial} y\phi_i \boldsymbol{n} \cdot \boldsymbol{f}(u) = 0, \tag{5}$$

where the superscript ∂ indicates the restriction to the boundary $\partial\Omega$ of the domain Ω, $\partial\Omega_i^\partial \equiv \partial\Omega_i \cap \partial\Omega$ and where the fact that the basis function ϕ_i of any node i vanishes on the boundary of $\partial\Omega_i$ of its support Ω_i, but for the nodes lying on the boundary, is accounted for.

The boundary integral in (5) can be split into an integral along the axis of symmetry, $\partial\Omega_{\text{axis}}$, and a contribution pertaining the remaining portion of $\partial\Omega$, $\partial\Omega\backslash\partial\Omega_{\text{axis}}$, see Fig. 1, as follows

$$\int_{\partial\Omega_i^\partial} y\phi_i \boldsymbol{n} \cdot \boldsymbol{f}(u) = \int_{\partial\Omega_i^\partial \cap \partial\Omega_{\text{axis}}} y\phi_i \boldsymbol{n} \cdot \boldsymbol{f}(u) + \int_{\partial\Omega_i^\partial \cap (\partial\Omega\backslash\partial\Omega_{\text{axis}})} y\phi_i \boldsymbol{n} \cdot \boldsymbol{f}(u) = \int_{\partial\Omega_i^\partial \cap (\partial\Omega\backslash\partial\Omega_{\text{axis}})} y\phi_i \boldsymbol{n} \cdot \boldsymbol{f}(u)$$

since the integral along $\partial\Omega_{\text{axis}}$ ($y = 0$) is identically zero. Therefore, the weak form of (3) satisfies the properties (4) of vanishing normal fluxes at the axis, where $\boldsymbol{n} = \hat{\boldsymbol{y}}$, in an integral sense. To simplify the presentation of the theory and the implementation of the numerical scheme into a computer code, in the following the distinction between the axis of symmetry and the remaining part of the boundary will not be indicated explicitly. This choice allows also to deal with geometries not including the axis with no changes in the equations.

Following the standard (Bubnov–) Galerkin approach, the solution $u(\boldsymbol{x}, t)$ is now approximated by the function $u_h(\boldsymbol{x}, t)$ obtained by an expansion in the same space of the weighting functions $\phi_h(\boldsymbol{x})$ as follows:

$$u(\boldsymbol{x}, t) \simeq u_h(\boldsymbol{x}, t) = \sum_{k \in \mathscr{K}} u_k(t)\phi_k(\boldsymbol{x}),$$

where $u_k(t)$ is the value at node k of the approximate solution at time t. Substituting the expansion of u_h into (5) gives

$$\sum_{k\in\mathscr{K}_i} M^y_{ik}\frac{\mathrm{d}u_k}{\mathrm{d}t} = \int_{\Omega_i} y\boldsymbol{f}(u_h)\cdot\nabla\phi_i - \int_{\partial\Omega_i^\partial} y\phi_i\boldsymbol{n}\cdot\boldsymbol{f}(u_h), \tag{6}$$

where $\mathscr{K}_i$ is the set of shape functions ϕ_k whose support Ω_k overlaps the support Ω_i of ϕ_i, namely, $\Omega_{ik}\equiv\Omega_i\cap\Omega_k\neq\emptyset$. In Eq. (6) the definition of a mass matrix weighted with the distance y from the axis, namely,

$$M^y_{ik} = \int_{\Omega_{ik}} y\phi_i\phi_k, \tag{7}$$

has been introduced. Note that the above finite element discretization is closely linked to the weighted finite element technique [19,20].

The flux function is now reinterpolated [3,8,21] by means of the same basis functions ϕ_h, namely,

$$\boldsymbol{f}(u_h(\boldsymbol{x},t)) = \boldsymbol{f}\left(\sum_{k\in\mathscr{K}} u_k(t)\phi_k(\boldsymbol{x})\right) \simeq \sum_{k\in\mathscr{K}} \boldsymbol{f}_k(t)\phi_k(\boldsymbol{x}),$$

where $\boldsymbol{f}_k(t)\equiv\boldsymbol{f}(u_k(t))$. Such an approximation, often referred to as "group representation" of "flux reinterpolation", introduces an integration error whose analysis is beyond the scope of this work; the reader is referred to the book of Donea and Huerta [21] for a detailed error analysis.

Finally, the discrete Galerkin formulation of the conservation law reads

$$\sum_{k\in\mathscr{K}_i} M^y_{ik}\frac{\mathrm{d}u_k}{\mathrm{d}t} = \sum_{k\in\mathscr{K}_i} \boldsymbol{f}_k\cdot\int_{\Omega_{ik}} y\phi_k\nabla\phi_i - \sum_{k\in\mathscr{K}_i^\partial} \boldsymbol{f}_k\cdot\int_{\partial\Omega_{ik}^\partial} y\phi_i\phi_k\boldsymbol{n}, \tag{8}$$

where $\partial\Omega_{ik}^\partial = \partial\Omega_i\cap\partial\Omega_k\cap\partial\Omega$. The introduction of the flux reinterpolation allows us to recast the integrals in space involving the (time-dependent) flux function as the product of the time-dependent nodal value $\boldsymbol{f}_k(t)$ and spatial integrals involving the shape functions ϕ_i and ϕ_k, that depend only on the mesh geometry. Therefore, the computation of the integrals can be performed once and for all at the beginning of the computation, in a preprocessing phase. This leads to a significant reduction in the CPU time requirements with respect to the standard Galerkin approach (cf. Eq. (6)).

The spatially discrete equation (8) is now further manipulated to recast the numerical scheme in the node-pair form introduced by Selmin [3,8]. By substituting the two identities (A.1) and (A.2), to be demonstrated in Appendix A, into (8), the node-pair representation of the discrete equation is found to be

$$\sum_{k\in\mathscr{K}_i} M^y_{ik}\frac{\mathrm{d}u_k}{\mathrm{d}t} = -\sum_{k\in\mathscr{K}_{i,\neq}}\left[\frac{\boldsymbol{f}_i+\boldsymbol{f}_k}{2}\cdot\boldsymbol{\eta}^y_{ik} - \hat{\boldsymbol{y}}\cdot\frac{\boldsymbol{f}_k-\boldsymbol{f}_i}{2}M_{ik}\right] - \sum_{k\in\mathscr{K}^\partial_{i,\neq}}\frac{\boldsymbol{f}_k-\boldsymbol{f}_i}{2}\cdot\boldsymbol{\chi}^y_{ik} - \boldsymbol{f}_i\cdot\boldsymbol{\xi}^y_i, \tag{9}$$

where $\mathscr{K}_{i,\neq}\equiv\mathscr{K}_i\setminus\{i\}$ and $\mathscr{K}^\partial_{i,\neq}\equiv\mathscr{K}^\partial_i\setminus\{i\}$. In Eq. (9) the following basic *metric quantities,*

$$\begin{aligned}
M^y_{ik} &= \int_{\Omega_{ik}} y^\epsilon\phi_i\phi_k, \quad M_{ik} = \epsilon\int_{\Omega_{ik}}\phi_i\phi_k,\\
\boldsymbol{\eta}^y_{ik} &= \int_{\Omega_{ik}} y^\epsilon(\phi_i\nabla\phi_k - \phi_k\nabla\phi_i),\\
\boldsymbol{\chi}^y_{ik} &= \int_{\partial\Omega^\partial_{ik}} y^\epsilon\phi_i\phi_k\boldsymbol{n}, \quad \boldsymbol{\xi}^y_i = \int_{\partial\Omega^\partial_i} y^\epsilon\phi_i\boldsymbol{n},
\end{aligned} \tag{10}$$

have been introduced. In the definitions above, the parameter ϵ assumes the value $\epsilon=1$ for axisymmetric problems and $\epsilon=0$ for plane problems, respectively. In this way the relationship with the metric quantities originally conceived by Selmin [3] for the Cartesian equations for 2D and 3D problems is made clear: all integrals defining the scalar and vector metric quantities for axisymmetric equations contain the additional factor y. Moreover, it is necessary to consider *two* mass matrices: a first matrix, M^y_{ik}, is modified by the presence of the multiplying factor y in the integrand and is required to represent the evolutionary term of the equation, whereas the second matrix, M_{ik}, is the standard mass matrix and is necessary to account for the additional flux term stemming from the cylindrical coordinates. In any case, the expressions of the metric quantities

in (10) show that extending a Cartesian computer code to the axisymmetric cylindrical case is almost straightforward.

Note that property (4) of the governing equation at the axis of symmetry is satisfied by construction of the metric quantities. In fact, both $\boldsymbol{\chi}_{ik}^{y}$ and $\boldsymbol{\xi}_{i}^{y}$ are identically zero for those nodes i and k on the axis. The y-component of the integrated numerical fluxes is therefore identically zero at the axis of symmetry, in accordance with (4). This is a key feature of the scheme that allows to automatically account for the axis of symmetry without the need of including numerical switch or special treatments. This is not the case for example in the FV schemes proposed in [15,17], in which the condition of a zero normal flux at the axis of symmetry is imposed explicitly.

The node-pair representation of the discrete equations can be translated directly into a very efficient computer algorithm as follows. A list of the node-pairs i–k, namely, of those couples of nodes i and k of the triangulation with non-zero overlapping supports Ω_i and Ω_k (see Fig. 2) is built once and for all at the beginning of the computations, together with the corresponding metric quantities, which can be associated to either the node-pairs (such as $\boldsymbol{\eta}_{ik}^{y}$ and M_{ik}^{y}, $i \neq k$) or the domain (M_{ii}^{y}) or boundary ($\boldsymbol{\xi}_{i}^{y}$) nodes of the triangulation. At each discrete time level, the right-hand side of (9) is computed by looping on all couples i–k. For each couple, the node-pair contributions to the right-hand side are computed and accumulated into the positions pertaining to nodes i and k. Note that, in accordance with the conservative nature of the scheme, each node-pair contribution in (9) is antisymmetric with respect to i and k and it can be computed only once for each node-pair and accumulated in the right-hand side in both the ith position and, with opposite sign, the kth one. Finally, nodal contributions are computed.

To simplify the task of determining a correspondence between the finite element and the finite volume discretizations, an additional approximation is now introduced,

$$\sum_{k\in\mathscr{K}_i} M_{ik}^{y}\frac{\mathrm{d}u_i}{\mathrm{d}t} = L_i^{y}\frac{\mathrm{d}u_i}{\mathrm{d}t} + \sum_{k\in\mathscr{K}_{i,\neq}} M_{ik}^{y}\frac{\mathrm{d}(u_k-u_i)}{\mathrm{d}t} \simeq L_i^{y}\frac{\mathrm{d}u_i}{\mathrm{d}t} \tag{11}$$

with $L_i^{y} = \sum_{k\in\mathscr{K}_i} M_{ik}^{y}$, namely, the weighted mass matrix M_{ik}^{y} is diagonalized or "lumped", and Eq. (9) reads

$$L_i^{y}\frac{\mathrm{d}u_i}{\mathrm{d}t} = -\sum_{k\in\mathscr{K}_{i,\neq}}\left[\frac{\boldsymbol{f}_i+\boldsymbol{f}_k}{2}\cdot\boldsymbol{\eta}_{ik}^{y} - \hat{\boldsymbol{y}}\cdot\frac{\boldsymbol{f}_k-\boldsymbol{f}_i}{2}M_{ik}\right] - \sum_{k\in\mathscr{K}_{i,\neq}^{\partial}}\frac{\boldsymbol{f}_k-\boldsymbol{f}_i}{2}\cdot\boldsymbol{\chi}_{ik}^{y} - \boldsymbol{f}_i\cdot\boldsymbol{\xi}_i^{y}. \tag{12}$$

Such an approximation introduces a non-negligible (phase) error in time with respect to the standard finite element approach [21]. In fact, the solution of conservation laws in the finite element framework including the consistent mass matrix M_{ik}^{y} is still a subject of active research, see e.g. [22].

To conclude, it is to be recalled that initial conditions at time $t = 0$ and suitable boundary conditions at each discrete time level are to be provided for (3) to be solvable, see e.g. [16]. In the FE approximation considered here, boundary conditions are enforced in a "weak" sense, namely, by evaluating the fluxes occurring in the integrals along the boundary in some suitable state $\bar{u}$. The boundary value $\bar{u}$ depends in general on both the unknowns and the boundary data, that is, $\bar{u} = \bar{u}(u, b)$, with b boundary data. In particular, the boundary value $\bar{u}$ is equal to the boundary data b at inflow boundaries, namely, $\bar{u} = b$ if $\boldsymbol{a}(u)\cdot\boldsymbol{n} \leqslant 0$, with $\boldsymbol{a} = \mathrm{d}\boldsymbol{f}/\mathrm{d}u$ advection velocity, and to u at outflow boundaries ($\boldsymbol{a}(u)\cdot\boldsymbol{n} > 0$), in accordance with the hyperbolic nature

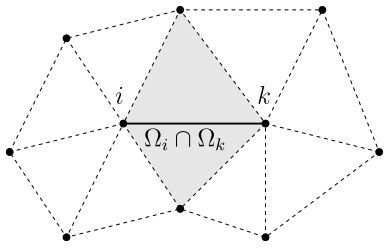

Fig. 2. Definition of the i–k node-pair associated with nodes i and k with overlapping supports Ω_i and Ω_k, respectively, for a grid made of linear finite elements of triangular shape. The shaded region is the intersection of Ω_i and Ω_k, namely, $\Omega_{ik} = \Omega_i \cap \Omega_k$. Dashed lines indicate the underlying finite element grid.

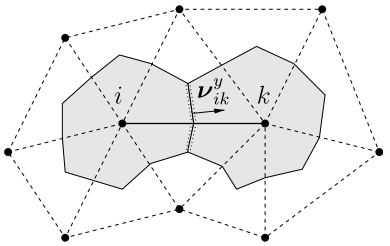

Fig. 3. Node-pair associated with the finite volume interface $\partial\mathscr{C}_{ik} = \partial\mathscr{C}_i \cap \partial\mathscr{C}_k$ and metric vector $\boldsymbol{\nu}^y_{ik}$ (integrated normal) in two spatial dimensions. The shape of the finite elements $\mathscr{C}_i$ and $\mathscr{C}_k$ (shaded region) is arbitrary. Dashed line indicate the underlying triangulation of the domain Ω.

of the governing equation. The reader is referred to [23] for a detailed description of the treatment of the boundary terms in the node-pair finite element framework. Though the axis is formally a boundary of the 2D x–y representation of the geometry, no boundary conditions are to be imposed at the axis of symmetry, which is in fact not a boundary in the original 3D problem (1), as discussed in Section 2.1. However, for simplicity in the computer implementation of the algorithm, the grid nodes along the axis of symmetry are not dealt with differently from the boundary nodes: the fulfillment of property (4) guarantees in fact the correct treatment of the axis for any value of $\bar{u}$ used in the computation of the boundary integrals at the axis.

2.3. Relation to the finite volume method

As an alternative to the finite element approach considered so far, a different discrete form of the governing equations is now derived by applying the node-centered finite volume method [24], to the following integral form of (3),

$$\frac{\mathrm{d}}{\mathrm{d}t}\int_{\mathscr{C}} y u(\boldsymbol{x},t) = -\oint_{\partial\mathscr{C}} y\boldsymbol{n}\cdot\boldsymbol{f}(u) \quad \forall \mathscr{C} \subseteq \Omega,$$

where $\boldsymbol{n}$ indicates the outward normal vector of the region $\mathscr{C} \subseteq \Omega$ and where the Gauss theorem was used to reduce the domain integral of the divergence of the flux function to a boundary integral. The discrete counterpart of the above equation is obtained by selecting a finite number of non-overlapping volumes $\mathscr{C}_i \subset \Omega$, with boundary $\partial\mathscr{C}_i$, such that $\bigcup_i \mathscr{C}_i \equiv \Omega$; each finite volume $\mathscr{C}_i$ surrounds a single node i of the triangulation of Ω, see Fig. 3, so that

$$\frac{\mathrm{d}}{\mathrm{d}t}\int_{\mathscr{C}_i} y u(\boldsymbol{x},t) = -\oint_{\partial\mathscr{C}_i} y\boldsymbol{n}_i\cdot\boldsymbol{f}(u) \quad \forall i \in \mathscr{K},$$

and $\boldsymbol{n}_i$ denotes the outward normal with respect to the volume $\mathscr{C}_i$. The unknown u is approximated over $\mathscr{C}_i$ by its cell-averaged value u_i, namely,

$$u(\boldsymbol{x},t) \simeq u_i(t) = \frac{1}{V_i}\int_{\mathscr{C}_i} u(\boldsymbol{x},t) \quad \forall \boldsymbol{x} \in \mathscr{C}_i,$$

where V_i is the value of the volume[1] of the ith cell $\mathscr{C}_i$, and therefore

$$V_i^y \frac{\mathrm{d}u_i}{\mathrm{d}t} = -\oint_{\partial\mathscr{C}_i} y\boldsymbol{n}_i\cdot\boldsymbol{f}(u) \quad \forall i \in \mathscr{K}, \tag{13}$$

with

$$V_i^y = \int_{\mathscr{C}_i} y.$$

[1] In 2D problems, the volume V_i is in fact the *area* of the plane cell $\mathscr{C}_i$ around node i shown in Fig. 3. In the following, to adhere with the standard finite volume nomenclature, the quantity V_i will be referred to as the volume of cell i.

The right-hand side of (13) is now rearranged so as to put into evidence the node-pair structure of the data, namely,

$$\oint_{\partial\mathscr{C}_i} y\boldsymbol{n}\cdot\boldsymbol{f}(u) = \sum_{k\in\mathscr{I}_{i,\neq}} \int_{\partial\mathscr{C}_{ik}} y\boldsymbol{n}_i\cdot\boldsymbol{f}(u) + \int_{\partial\mathscr{C}_i^{\partial}} y\boldsymbol{n}_i\cdot\boldsymbol{f}(u), \tag{14}$$

where $\mathscr{I}_{i,\neq}$ is the set of the finite volumes $\mathscr{C}_k$ sharing part of their boundary with $\mathscr{C}_i$, $\mathscr{C}_i$ excluded, namely, $\partial\mathscr{C}_{ik} = \partial\mathscr{C}_i \cap \partial\mathscr{C}_k \neq \emptyset$, $k \neq i$. Note that $\boldsymbol{n}_i = -\boldsymbol{n}_k$ over $\partial\mathscr{C}_i \cap \partial\mathscr{C}_k$. In the finite volume jargon, the set $\partial\mathscr{C}_i \cap \partial\mathscr{C}_k$ is often referred to as the *cell interface* between the volumes $\mathscr{C}_i$ and $\mathscr{C}_k$ (Fig. 3). The integrals in (14) are undefined at cell interfaces due to the piecewise constant approximation chosen for u, namely, the discrete unknown is discontinuous across $\partial\mathscr{C}_i \cap \partial\mathscr{C}_k$. If the flux function is assumed to be constant at cell interfaces and equal to its algebraic mean $(\boldsymbol{f}_k + \boldsymbol{f}_i)/2$, from (13) and (14) one has

$$V_i^y \frac{\mathrm{d}u_i}{\mathrm{d}t} = -\sum_{k\in\mathscr{I}_{i,\neq}} \frac{\boldsymbol{f}_i + \boldsymbol{f}_k}{2}\cdot\boldsymbol{v}_{ik}^y - \boldsymbol{f}_i\cdot\boldsymbol{v}_i^y, \tag{15}$$

where, according to the piecewise-constant approximation of the unknown, the boundary flux is assumed to be constant over $\partial\mathscr{C}_i \cap \partial\Omega$ and equal to its nodal value $\boldsymbol{f}_i$ and where

$$\boldsymbol{v}_{ik}^y = \int_{\partial\mathscr{C}_{ik}} y\boldsymbol{n}_i \quad \text{and} \quad \boldsymbol{v}_i^y = \int_{\partial\mathscr{C}_i^{\partial}} y\boldsymbol{n}_i.$$

Note that the domain metric vectors $\boldsymbol{v}_{ik}^y$ defined above are antisymmetric, namely, $\boldsymbol{v}_{ik}^y = -\boldsymbol{v}_{ki}^y$, a property that, together with the centered approximation $(\boldsymbol{f}_i + \boldsymbol{f}_k)/2$ of the fluxes at cell interfaces, guarantees that the scheme is conservative. A geometric conditions also exists relating the volume V_i of $\mathscr{C}_i$, $\boldsymbol{v}_{ik}^y$ and $\boldsymbol{v}_i^y$, that is, from the following identity (gradient theorem),

$$\int_{\mathscr{C}_i} \nabla y = \oint_{\partial\mathscr{C}_i} y\boldsymbol{n},$$

it follows that

$$V_i\hat{\boldsymbol{y}} - \sum_{k\in\mathscr{I}_{i,\neq}} \boldsymbol{v}_{ik}^y = 0 \quad \text{for any domain node } i, \tag{16a}$$

$$V_i\hat{\boldsymbol{y}} - \sum_{k\in\mathscr{I}_{i,\neq}} \boldsymbol{v}_{ik}^y = \boldsymbol{v}_i^y \quad \text{for any boundary node } i. \tag{16b}$$

The scheme (15) is now compared to the finite element approximation of the scalar conservation law (3). Remarkably enough, the expression of the mass-lumped approximation (12) is very similar to its finite volume counterpart (15); in fact, they are formally equivalent – provided that the finite element metric quantities L_i^y, $\boldsymbol{\eta}_{ik}^y$ and $\boldsymbol{\xi}_i^y$ can be linked to their finite volume counterparts V_i^y, $\boldsymbol{v}_{ik}^y$ and $\boldsymbol{v}_i^y$ – but for the presence in (12) of the domain term $\hat{\boldsymbol{y}}\cdot(\boldsymbol{f}_k - \boldsymbol{f}_i)M_{ik}/2$ and the boundary term $(\boldsymbol{f}_k - \boldsymbol{f}_i)\cdot\boldsymbol{\chi}_{ik}^y/2$, which are regarded here as higher-order corrections to (15) stemming form the piecewise linear finite element representation of the unknown. Note that the higher-order corrections vanish if these contributions are diagonalized or lumped.

The relation between the FE and FV metric quantities is now demonstrated. First, it is to be noted that both $\boldsymbol{\eta}_{ik}^y$ and $\boldsymbol{v}_{ik}^y$ are antisymmetric with respect to i and k, namely, $\boldsymbol{\eta}_{ik}^y = -\boldsymbol{\eta}_{ki}^y$ and $\boldsymbol{v}_{ik}^y = -\boldsymbol{v}_{ki}^y$. It remains to be proved that the finite element metric quantities satisfy the geometric conditions (16). The above is easily demonstrated by recalling identity (A.6), namely,

$$\sum_{k\in\mathscr{K}_i} [\boldsymbol{\eta}_{ik}^y - M_{ik}\hat{\boldsymbol{y}} + \boldsymbol{\chi}_{ik}^y] = 0.$$

From the shape function property $\sum_{k\in\mathscr{K}_i}\phi_k(\boldsymbol{x}) \equiv 1\ \forall\boldsymbol{x}\in\Omega_i$ and from definitions (10), one also has

$$\sum_{k\in\mathscr{K}_i} \boldsymbol{\chi}_{ik}^y = \sum_{k\in\mathscr{K}_i} \int_{\partial\Omega_i^{\partial}} y\phi_i\phi_k\boldsymbol{n} = \int_{\partial\Omega_i^{\partial}} y\phi_i\left(\sum_{k\in\mathscr{K}_i}\phi_k\right)\boldsymbol{n} = \int_{\partial\Omega_i^{\partial}} y\phi_i\boldsymbol{n} = \boldsymbol{\xi}_i^y,$$

and therefore

$$L_i\hat{\boldsymbol{y}} - \sum_{k\in\mathscr{K}_i} \boldsymbol{\eta}^y_{ik} = \boldsymbol{\xi}^y_i$$

with $L_i = \sum_{k\in\mathscr{K}_i} M_{ik}$ lumped mass matrix. The boundary metric vector $\boldsymbol{\xi}^y_i$ differs from zero only if i belongs to the boundary, namely, if $i \in \mathscr{K}^{\partial}$, and hence (cf. properties (16)),

$$L_i\hat{\boldsymbol{y}} - \sum_{k\in\mathscr{K}_{i,\neq}} \boldsymbol{\eta}^y_{ik} = 0 \quad \text{for any domain node } i, \tag{17a}$$

$$L_i\hat{\boldsymbol{y}} - \sum_{k\in\mathscr{K}_{i,\neq}} \boldsymbol{\eta}^y_{ik} = \boldsymbol{\xi}^y_i \quad \text{for any boundary node } i. \tag{17b}$$

Therefore, a FV approximation to (3) can be formally constructed using the FE metric quantities defined in (10) by setting

$$\begin{aligned} \mathscr{I}_{i,\neq} &= \mathscr{K}_{i,\neq}, \quad V^y_i = L^y_i, \quad \boldsymbol{v}^y_{ik} = \boldsymbol{\eta}^y_{ik}, \\ V_i &= L_i, \qquad \boldsymbol{v}^y_i = \boldsymbol{\xi}^y_i. \end{aligned} \tag{18}$$

Note that $\sum_{i\in\mathscr{K}} L_i \equiv |\,\Omega\,| \equiv \sum_{i\in\mathscr{K}} V_i$ is the volume of the domain Ω.

It is worth noticing that the finite volumes respecting the FE/FV equivalence conditions (18) are different from those of simple shape – bounded by the segments connecting the midpoints of the edges to the center of gravity of the triangle – valid for the Cartesian case addressed by Selmin [3]. This can be easily demonstrated by considering the reference triangular element with vertices $(0,0)$, $(1,0)$ and $(0,1)$. However, the knowledge of the equivalent finite volume respecting the metrics in (18) is not necessary for constructing the discrete equations.

The equivalence between the finite element and the finite volume approach demonstrated above opens the way to the development of hybrid finite element/volume approximations for axially symmetric problems. Standard stabilization techniques developed in the finite volume framework, such as first-order upwind schemes or TVD schemes, are now available in the higher-order finite element framework. Conversely, higher-order finite element terms can be added to the discrete equations to improve the accuracy of existing finite volume discretizations.

3. The Euler equations for compressible flows

In Appendix B, the Euler equations for axisymmetric problems – including a possibly non-zero tangential velocity (swirling flows) – are derived. For simplicity, the case with zero tangential velocity, namely,

$$\frac{\partial[y\mathsf{u}]}{\partial t} + \boldsymbol{\nabla}\cdot[y\mathbf{f}(\mathsf{u})] = \mathsf{s}(\mathsf{u}), \tag{19}$$

is considered first, where u, $\mathsf{u} = (\rho, \boldsymbol{m}, E^{\mathrm{t}})$, is the vector unknown of the density $\rho \in \mathbb{R}^+$, momentum vector $\boldsymbol{m}$, $\boldsymbol{m} = (m_x, m_y) \in \mathbb{R}^2$ with m_x and m_y axial and radial components of the momentum density, respectively, and total energy per unit volume $E^{\mathrm{t}} \in \mathbb{R}$; $\mathbf{f}(\mathsf{u})$, $\mathbf{f} \in \mathbb{R}^4 \times \mathbb{R}^2$, is the Euler flux function to be defined in (20) and where it is understood that $\boldsymbol{\nabla}\cdot\mathbf{f} = \partial \mathsf{f}_x/\partial x + \partial \mathsf{f}_y/\partial y$, with $\mathsf{f}_x, \mathsf{f}_y \in \mathbb{R}^4$ vector components of $\mathbf{f}$ in the axial and radial directions, respectively. The solution of (19) is sought for in the spatial domain $\Omega \in \mathbb{R}^2$, with boundary $\partial\Omega$ for all times $t \in \mathbb{R}^+$. System (19) is made complete by specifying initial and boundary conditions as detailed in [16]. The flux function $\mathbf{f}$ is defined as

$$\mathbf{f}(\mathsf{u}) = \left(\boldsymbol{m}, \frac{\boldsymbol{m}\otimes\boldsymbol{m}}{\rho} + \Pi(\mathsf{u})\boldsymbol{I}, [E^{\mathrm{t}} + \Pi(\mathsf{u})]\frac{\boldsymbol{m}}{\rho}\right)^{\mathrm{T}}, \tag{20}$$

where $\boldsymbol{I}$ is the 2×2 identity matrix and where from the pressure equation of state $P = P(e,\rho)$, e internal energy per unit mass, the following *pressure function* $\Pi(\mathsf{u})$ in terms of the conservative variables, namely,

$$\Pi(\mathsf{u}) = \Pi(\rho, \boldsymbol{m}, E^{\mathrm{t}}) = P\left(\frac{E^{\mathrm{t}}}{\rho} - \frac{1}{2}\frac{|\boldsymbol{m}|^2}{\rho^2}, \rho\right),$$

has been introduced. The thermodynamic information required to write the pressure equations of state $P(e,\rho)$ can be obtained by specifying for example the two (compatible) equations of state for the pressure, $P = P(T,v)$, and for the internal energy, $e = e(T,v)$, as a function of the temperature T and the specific volume v; together, these equations of state define a complete thermodynamic model [25,26]. For the polytropic, i.e., constant specific heats, ideal gas considered here one has $P = RT\rho$, with R gas constant, and $e = RT/(\gamma - 1)$ and therefore

$$\Pi(\mathsf{u}) = (\gamma - 1)\left[E^{\mathrm{t}} - \frac{|\boldsymbol{m}|^2}{2\rho}\right],$$

where γ is the ratio $c_{\mathrm{P}}/c_{\mathrm{v}}$ of the specific heats at constant pressure and volume, respectively. In Eq. (19), $\mathsf{s} \in \mathbb{R}^4$ is the source term, which for zero tangential velocity reads (cf. definition (B.5) for swirling flows)

$$\mathsf{s}(\mathsf{u}) = (0, 0, \Pi(\mathsf{u}), 0)^{\mathrm{T}}. \tag{21}$$

3.1. The axis of symmetry

As observed in Section 2, the choice of a cylindrical coordinate system (x, y, θ), with θ angular coordinate, introduces a singularity at $y = 0$, namely, along the axis of symmetry, which remains to be investigated. The simple argument followed in Section 2 for a scalar conservation law with no source term is not applicable to the case of the Euler equations (19), whose behavior in the limit $y \to 0$ is studied as follows.

In Fig. 4, an axisymmetric three-dimensional control volume $\Omega^{3\mathrm{D}}$ bounded by the axis in cylindrical coordinates (the volume ABCDEF) is shown together with its axisymmetric representation Ω (the shaded rectangle ABCD, here referred to as the corresponding axisymmetric "volume"). According to the integral form of the Euler equations in three spatial dimensions, see e.g. [16], the change of any conserved quantity (density, momentum or total energy) in a given three-dimensional volume $\Omega^{3\mathrm{D}}$ is to be balanced by the corresponding flux along its surface $\partial\Omega^{3\mathrm{D}}$, namely, the time derivative of the integral over the volume ABCDEF of the conserved variable is equal to the sum of the surface integrals on ABCD, ABFE, CDEF, BFC, AED and AB of the flux function times the outward normal to the surface. The integral along surface AB is identically zero in the case under examination, because, although the integrand function can be possibly different from zero, the area of surface AB is zero, namely,

$$\int_{\partial\Omega^{3\mathrm{D}}_{\mathrm{AB}}} \mathbf{f}(\mathsf{u}) \cdot \boldsymbol{n} \equiv 0,$$

where the superscript 3D indicates integration in the three-dimensional space. The above clearly holds for any axisymmetric control volume bounded by the axis of symmetry. It is therefore appropriate to check whether the (reduced) system (19) verifies the above property of a zero contribution of the boundary integrals of the fluxes along the axis of symmetry. In fact, for the prototypical rectangle ABCD in Fig. 4, one has

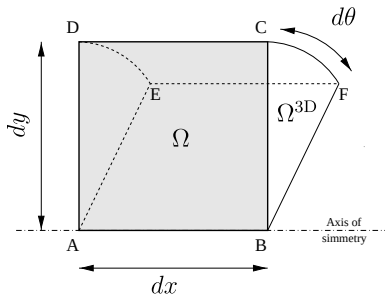

Fig. 4. Three-dimensional control volume $\Omega^{3\mathrm{D}}$ (ABCDEF), with volume $\mathrm{d}x(\mathrm{d}y)^2\,\mathrm{d}\theta$, and its two-dimensional axisymmetric counterpart Ω (ABCD), with "volume" (area) $\mathrm{d}x\,\mathrm{d}y$.

$$\int_{\partial\Omega_{\mathrm{AB}}} y\mathbf{f}(\mathsf{u})\cdot\boldsymbol{n} = \int_{x_{\mathrm{A}}}^{x_{\mathrm{B}}} 0\mathbf{f}(\mathsf{u})\cdot\boldsymbol{n} \equiv 0,$$

as in the fully three-dimensional case. In other words, in the reduced axisymmetric form of the Euler equations, the boundary integrals along the axis of symmetry are identically zero because the integrands are zero at $y = 0$, irrespective of the fact that length of the segment AB is not zero, or, with reference to Fig. 1,

$$\int_{\partial\Omega\subset\partial\Omega_{\mathrm{axis}}} y\mathbf{f}(\mathsf{u})\cdot\boldsymbol{n} \equiv 0 \quad \forall\partial\Omega\subset\partial\Omega_{\mathrm{axis}}. \tag{22}$$

In the next section, the spatially discrete form of the Euler equation (19) is obtained by means of the FE method and the FV method both formulated in the node-pair format. Boundary conditions and the treatment of the axis of symmetry are discussed in Section 3.3, where the above property of the governing equations will be found to be satisfied also by the discrete equations.

3.2. Node-pair finite element/volume discretization

The Euler equations (19) are now recast in a weak or variational form according to the procedure detailed in Section 2 as follows:

$$\int_{\Omega_i} y\phi_i\frac{\partial\mathsf{u}}{\partial t} - \int_{\Omega_i} y\mathbf{f}(\mathsf{u})\cdot\nabla\phi_i + \int_{\partial\Omega_i^{\partial}} y\phi_i\boldsymbol{n}\cdot\mathbf{f}(\mathsf{u}) = \int_{\Omega_i}\phi_i\mathsf{s}(\mathsf{u}). \tag{23}$$

By introducing the FE approximation of the vector unknown u_h and the group representation [3,8,21] of both the flux function $\mathbf{f}$ and of the source term s, namely,

$$\begin{aligned}
\mathsf{u}(\boldsymbol{x},t) &\simeq \mathsf{u}_h(\boldsymbol{x},t) = \sum_{k\in\mathscr{K}}\mathsf{u}_k(t)\phi_k(\boldsymbol{x}),\\
\mathbf{f}(\mathsf{u}_h(\boldsymbol{x},t)) &\simeq \mathbf{f}_h(\boldsymbol{x},t) = \sum_{k\in\mathscr{K}}\mathbf{f}_k(t)\phi_k(\boldsymbol{x})\\
\mathsf{s}(\mathsf{u}_h(\boldsymbol{x},t)) &\simeq \mathsf{s}_h(\boldsymbol{x},t) = \sum_{k\in\mathscr{K}}\mathsf{s}_k(t)\phi_k(\boldsymbol{x}),
\end{aligned}$$

where $\mathbf{f}_k(t)\equiv\mathbf{f}(\mathsf{u}_k(t))$ and $\mathsf{s}_k(t)\equiv\mathsf{s}(\mathsf{u}_k(t))\equiv(0,0,\Pi(\mathsf{u}_k),0)^{\mathrm{T}}$, the node-pair centered lumped FE approximation to the Euler equations (19) is obtained as follows:

$$L_i^y\frac{\mathrm{d}\mathsf{u}_i}{\mathrm{d}t} = -\sum_{k\in\mathscr{K}_{i,\neq}}\left[\frac{\mathbf{f}_i+\mathbf{f}_k}{2}\cdot\boldsymbol{\eta}_{ik}^y - \hat{\boldsymbol{y}}\cdot\frac{\mathbf{f}_k-\mathbf{f}_i}{2}M_{ik}\right] + \sum_{k\in\mathscr{K}_i} M_{ik}\mathsf{s}_k - \sum_{k\in\mathscr{K}_{i,\neq}^{\partial}}\frac{\mathbf{f}_k-\mathbf{f}_i}{2}\cdot\boldsymbol{\chi}_{ik}^y - \mathbf{f}_i\cdot\boldsymbol{\xi}_i^y, \tag{24}$$

where the FE metric quantities are defined in (10). The corresponding FV discretization of the Euler equations is given by (cf. Section 2.3)

$$L_i^y\frac{\mathrm{d}\mathsf{u}_i}{\mathrm{d}t} = -\sum_{k\in\mathscr{K}_{i,\neq}}\frac{\mathbf{f}_i+\mathbf{f}_k}{2}\cdot\boldsymbol{\eta}_{ik}^y + L_i\mathsf{s}_i - \mathbf{f}_i\cdot\boldsymbol{\xi}_i^y, \tag{25}$$

where, in accordance to the piecewise constant FV representation of the unknowns the source term assumes the constant value $\mathsf{s}_i = \mathsf{s}(\mathsf{u}_i)$ over the ith control volume. As observed in the scalar case in Section 2, the difference between the FV and the lumped FE scheme is given by the high-order FE domain and boundary terms $\frac{1}{2}\sum_{k\in\mathscr{K}_{i,\neq}}\hat{\boldsymbol{y}}\cdot[\mathbf{f}_k-\mathbf{f}_i]M_{ik}$ and $\frac{1}{2}\sum_{k\in\mathscr{K}_{i,\neq}^{\partial}}[\mathbf{f}_k-\mathbf{f}_i]\cdot\boldsymbol{\chi}_{ik}^y$, respectively.

The numerical scheme for the Euler equations for axisymmetric swirling flows is detailed in Appendix B.

3.3. Boundary conditions and the treatment of the axis of symmetry

Boundary conditions are enforced here in a "weak" sense by computing the boundary integral in some suitable boundary state $\overline{\mathsf{u}}$, which in general depends on the solution unknown u and on the boundary data b. All kinds of boundary conditions, including inflow/outflow or wall/symmetry (slip) boundary conditions can be

imposed by suitably selecting $\bar{\mathsf{u}}$; the former can be enforced by characteristic reconstruction of $\bar{\mathsf{u}}$ from the boundary data b and the value of the vector unknown u at the boundary node; the latter are easily imposed by subtracting from u the component of the momentum vector normal to the boundary. A detailed description of boundary treatment within the node-pair framework is given in [23].

As in the scalar case of Section 2, it is remarkable that the discrete equations (24) and (25) satisfy property (22) at the axis of symmetry. In fact, by inspection of the metric property definitions (10), one can easily note that all boundary metric quantities vanish at the axis of symmetry and therefore, in accordance with property (22), the boundary contribution to the discrete equations pertaining the axis of symmetry is identically zero under both the FE and FV approximations. Remarkably enough, the boundary node-pair contribution associated with the metric vector $\boldsymbol{\chi}^{y}_{ik}$ vanishes only provided that both nodes i and k of the node-pair are on the axis of symmetry.

4. Finite element/volume high-resolutions schemes

Two TVD schemes [12] are now derived as a suitable combination of the first order FV Roe upwind scheme [11], to be used near flow discontinuities, and the high-order FV scheme (25) or the FE scheme (24), to be used in regions of smooth flow. The two schemes are presented in Sections 4.1 and 4.2, respectively, for the Euler equations (19). The corresponding schemes for the scalar conservation law (1) are easily recovered as the special cases for a single unknown and are therefore not detailed in the following. In what follows, the source term is neglected for simplicity and is reintroduced in Section 4.3.

4.1. Finite volume TVD scheme

The first high-resolution scheme is now derived as a suitable combination of the second-order centered (25) and the Roe first-order upwind FV schemes. The latter reads [11,16]

$$L^{y}_{i}\frac{\mathrm{d}\mathsf{u}_i}{\mathrm{d}t} = -\sum_{k\in\mathscr{K}_{i,\neq}}\left[\frac{\mathbf{f}_i+\mathbf{f}_k}{2}\cdot\boldsymbol{\eta}^{y}_{ik} - \frac{1}{2}|\tilde{\mathsf{A}}^{\boldsymbol{\eta}}_{ik}|(\mathsf{u}_k-\mathsf{u}_i)\right] - \mathbf{f}_i\cdot\boldsymbol{\xi}^{y}_{i}, \tag{26}$$

where the Roe matrix $|\tilde{\mathsf{A}}^{\boldsymbol{\eta}}_{ik}|\in\mathbb{R}^4\times\mathbb{R}^4$ satisfies the following condition:

$$\tilde{\mathsf{A}}^{\boldsymbol{\eta}}_{ik}(\mathsf{u}_k-\mathsf{u}_i) = [\mathbf{f}_k-\mathbf{f}_i]\cdot\boldsymbol{\eta}^{y}_{ik} \tag{27}$$

In (26), $|\tilde{\mathsf{A}}^{\boldsymbol{\eta}}_{ik}| = \tilde{\mathsf{R}}^{\boldsymbol{\eta}}_{ik}\,|\tilde{\Lambda}^{\boldsymbol{\eta}}_{ik}|\,\tilde{\mathsf{L}}^{\boldsymbol{\eta}}_{ik}$, with $\tilde{\mathsf{R}}^{\boldsymbol{\eta}}_{ik}$ and $\tilde{\mathsf{L}}^{\boldsymbol{\eta}}_{ik}$ matrices of the right and left eigenvectors of $\tilde{\mathsf{A}}^{\boldsymbol{\eta}}_{ik}$, respectively, and $|\tilde{\Lambda}^{\boldsymbol{\eta}}_{ik}| = \mathrm{diag}(|\tilde{\lambda}^{\boldsymbol{\eta}}_{ik}|)$, $\tilde{\lambda}^{\boldsymbol{\eta}}_{ik}\in\mathbb{R}^4$ vector of the eigenvalues of $\tilde{\mathsf{A}}^{\boldsymbol{\eta}}_{ik}$. A review of different techniques to devise a Roe matrix for general, namely, non-ideal, thermodynamic models can be found for example in [27,28].

A limiter diagonal matrix $\Psi_{ik}\in\mathbb{R}^4\times\mathbb{R}^4$ is introduced to switch between the first-order and the second-order approximation as follows, see e.g. [24],

$$\begin{aligned}
L^{y}_{i}\frac{\mathrm{d}\mathsf{u}_i}{\mathrm{d}t} &= -\frac{1}{2}\sum_{k\in\mathscr{K}_{i,\neq}}\left[(\mathbf{f}_i+\mathbf{f}_k)\cdot\boldsymbol{\eta}^{y}_{ik} + (\Psi_{ik}-\mathsf{I})|\tilde{\mathsf{A}}^{\boldsymbol{\eta}}_{ik}|(\mathsf{u}_k-\mathsf{u}_i)\right] - \mathbf{f}_i\cdot\boldsymbol{\xi}^{y}_{i},\\
&= -\frac{1}{2}\sum_{k\in\mathscr{K}_{i,\neq}}\left[(\mathbf{f}_i+\mathbf{f}_k)\cdot\boldsymbol{\eta}^{y}_{ik} + (\Psi_{ik}-\mathsf{I})\tilde{\mathsf{R}}^{\boldsymbol{\eta}}_{ik}|\tilde{\Lambda}^{\boldsymbol{\eta}}_{ik}|\tilde{\mathsf{L}}^{\boldsymbol{\eta}}_{ik}(\mathsf{u}_k-\mathsf{u}_i)\right] - \mathbf{f}_i\cdot\boldsymbol{\xi}^{y}_{i},\\
&= -\frac{1}{2}\sum_{k\in\mathscr{K}_{i,\neq}}\left[(\mathbf{f}_i+\mathbf{f}_k)\cdot\boldsymbol{\eta}^{y}_{ik} + \tilde{\mathsf{R}}^{\boldsymbol{\eta}}_{ik}|\tilde{\Lambda}^{\boldsymbol{\eta}}_{ik}|(\tilde{\mathsf{w}}^{\boldsymbol{\eta}}_{ik}-\tilde{\mathsf{v}}^{\boldsymbol{\eta}}_{ik})\right] - \mathbf{f}_i\cdot\boldsymbol{\xi}^{y}_{i},
\end{aligned}$$

where I is the identity matrix of order four and where

$$\begin{aligned}
\tilde{\mathsf{v}}^{\boldsymbol{\eta}}_{ik} &= \tilde{\mathsf{L}}^{\boldsymbol{\eta}}_{ik}(\mathsf{u}_k-\mathsf{u}_i),\\
\tilde{\mathsf{w}}^{\boldsymbol{\eta}}_{ik} &= \Psi_{ik}\tilde{\mathsf{v}}^{\boldsymbol{\eta}}_{ik} = \Psi_{ik}\tilde{\mathsf{L}}^{\boldsymbol{\eta}}_{ik}(\mathsf{u}_k-\mathsf{u}_i)
\end{aligned} \tag{28}$$

are the so-called centered and limited "characteristic jump", a nomenclature that roots in the locally linearized form of (19) obtained via the Roe linearization technique. Note that the above relation reduces to the first order scheme (26) for $\Psi_{ik}=0$, whereas for $\Psi_{ik}=\mathsf{I}$ the second-order centered scheme (25) is recovered (for $\mathsf{s}\equiv 0$). By substituting the van Leer limiter [10] considered here, one has

$$\tilde{w}^{\eta}_{ik,p} = \frac{\tilde{v}^{\eta}_{ik,p}|\tilde{q}^{\eta}_{ik,p}| + \tilde{q}^{\eta}_{ik,p}|\tilde{v}^{\eta}_{ik,p}|}{|\tilde{v}^{\eta}_{ik,p}| + |\tilde{q}^{\eta}_{ik,p}| + \epsilon}, \tag{29}$$

where the subscript p indicates the pth component of each vector and ϵ is a small positive parameter introduced here to avoid division by zero of a zero quantity ($\epsilon = 10^{-12}$ in the computations). The pth component of the vector of "upwind" jumps $\tilde{q}^{\eta}_{ik}$ is given by

$$\tilde{q}^{\eta}_{ik,p} = \begin{cases} \tilde{L}^{\eta}_{ik,p}(u_{k\star} - u_k) & \text{if } \tilde{\lambda}^{\eta}_{ik,p} > 0, \\ \tilde{L}^{\eta}_{ik,p}(u_i - u_{i\star}) & \text{if } \tilde{\lambda}^{\eta}_{ik,p} \leqslant 0. \end{cases} \tag{30}$$

In the definition above, states $u_{i\star}$ and $u_{k\star}$ are the so-called upwind states associated to node-pair i–k and $\tilde{L}^{\eta}_{ik,p}$ is the pth row of matrix $\tilde{L}^{\eta}_{ik}$. Following [29], the upwind states $u_{i\star}$ and $u_{k\star}$ are the values of the solution unknown in the two grid nodes $i^{\star}$ and $k^{\star}$, respectively, that belong to the two node-pairs best aligned with i–k, as shown in Fig. 5. Other options are available and reviewed in [30], where the upwind values of the unknowns are found by either extrapolating from states u_i and u_k or interpolating on the upwind grid element.

Definitions (28) provide the implicit definition of the limiter function Ψ_{ik}, namely, $\tilde{w}^{\eta}_{ik} = \Psi_{ik}\tilde{v}^{\eta}_{ik}$, that is found to be a function of the four states $u_{i\star}$, u_i, u_k and $u_{k\star}$. From (29), the (p,p) element of the diagonal matrix Ψ_{ik} therefore reads

$$\Psi_{ik,p} = \frac{\tilde{w}^{\eta}_{ik,p}}{\tilde{v}^{\eta}_{ik,p}} = \frac{\theta + |\theta|}{1 + |\theta|},$$

with $\theta = \tilde{q}^{\eta}_{ik,p}/\tilde{v}^{\eta}_{ik,p}$ namely, the van Leer limiter as originally proposed in [10]. Note that the above expression of the limiter function becomes singular for $\tilde{v}^{\eta}_{ik,p} = 0$, whereas the expression for the limited characteristic jumps (29) gives the correct value of $\tilde{w}^{\eta}_{ik,p} = 0$ for $\tilde{v}^{\eta}_{ik,p} = 0$.

4.2. Hybrid finite element/volume TVD scheme

The hybrid finite element/volume TVD scheme is now obtained as a limited combination of the mass-lumped finite element scheme (24) and the first-order upwind scheme (26). Differently from the centered/upwind scheme presented in the previous section, the boundary terms of the two schemes are not the same and a suitable limiting technique is to be devised. The same holds also for the domain term $\hat{\boldsymbol{y}} \cdot (\mathbf{f}_k - \mathbf{f}_i)M_{ik}/2$, which is present in the FE scheme only. The general form of the high-resolution scheme reads

$$L^{y}_i \frac{\mathrm{d}u_i}{\mathrm{d}t} = -\frac{1}{2}\sum_{k\in\mathscr{K}_{i,\neq}} [(\mathbf{f}_i + \mathbf{f}_k)\cdot\boldsymbol{\eta}^{y}_{ik} + (\Psi_{ik} - \mathsf{I})|\tilde{A}^{\eta}_{ik}|(u_k - u_i) - \Psi^{\hat{y}}_{ik}\hat{\boldsymbol{y}}\cdot(\mathbf{f}_k - \mathbf{f}_i)M_{ik}] - \frac{1}{2}\sum_{k\in\mathscr{K}^{\circlearrowleft}_{i,\neq}} \Psi^{\chi}_{ik}(\mathbf{f}_k - \mathbf{f}_i)\cdot\boldsymbol{\chi}^{y}_{ik} - \mathbf{f}_i\cdot\boldsymbol{\xi}^{y}_i,$$

where the diagonal matrices $\Psi^{\hat{y}}_{ik}$ and Ψ^{χ}_{ik}, $\Psi^{\hat{y}}_{ik}$, $\Psi^{\chi}_{ik} \in \mathbb{R}^4 \times \mathbb{R}^4$, are additional limiter functions, which can possibly differ from the limiter Ψ_{ik} defined in the previous section. For $\Psi_{ik} = \Psi^{\hat{y}}_{ik} = \Psi^{\chi}_{ik} = \mathsf{I}$, the FE scheme (24) is recovered, whereas for $\Psi_{ik} = \Psi^{\hat{y}}_{ik} = \Psi^{\chi}_{ik} = 0$ the scheme above reduces to the first-order upwind scheme (26).

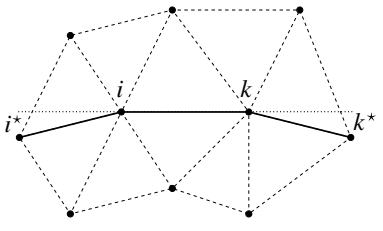

Fig. 5. Extended node-pair structure for high-resolution. Dashed lines indicate the underlying triangulation.

To find a suitable form for the functions $\Psi_{ik}^{\hat{y}}$ and Ψ_{ik}^{χ}, the definition (27) of the Roe matrix is generalized to a given direction vector $\boldsymbol{\omega} \in \mathbb{R}^2$ as follows:

$$\tilde{\mathsf{A}}_{ik}^{\omega}(\mathsf{u}_k - \mathsf{u}_i) = (\mathbf{f}_k - \mathbf{f}_i) \cdot \boldsymbol{\omega}. \tag{31}$$

It is now possible to introduce two new Roe matrices $\tilde{\mathsf{A}}_{ik}^{\hat{y}}$ and $\tilde{\mathsf{A}}_{ik}^{\chi}$ satisfying the linearization condition (31) along the directions identified by the vectors $\hat{\boldsymbol{y}}$ and $\boldsymbol{\chi}_{ik}^{y}$, respectively,

$$(\mathbf{f}_k/\mathbf{f}_i)\hat{\boldsymbol{y}} = \tilde{\mathsf{A}}_{ik}^{\hat{y}}(\mathsf{u}_k - \mathsf{u}_i) \quad \text{and} \quad (\mathbf{f}_k - \mathbf{f}_i) \cdot \boldsymbol{\chi}_{ik}^{y} = \tilde{\mathsf{A}}_{ik}^{\chi}(\mathsf{u}_k - \mathsf{u}_i)$$

and therefore the limiting procedure described in the previous section can be applied also to the FE contributions to give

$$L_i^y \frac{\mathrm{d}\mathsf{u}_i}{\mathrm{d}t} = -\frac{1}{2} \sum_{k \in \mathscr{K}_{i,\neq}} [(\mathbf{f}_i + \mathbf{f}_k) \cdot \boldsymbol{\eta}_{ik}^{y} + \tilde{\mathsf{R}}_{ik}^{\eta} |\tilde{\Lambda}_{ik}^{\eta}| (\tilde{\mathsf{w}}_{ik}^{\eta} - \tilde{\mathsf{v}}_{ik}^{\eta}) - M_{ik} \tilde{\mathsf{R}}_{ik}^{\hat{y}} \tilde{\Lambda}_{ik}^{\hat{y}} \tilde{\mathsf{w}}_{ik}^{\hat{y}}] - \frac{1}{2} \sum_{k \in \mathscr{K}_{i,\neq}^{\partial}} \tilde{\mathsf{R}}_{ik}^{\chi} \tilde{\Lambda}_{ik}^{\chi} \tilde{\mathsf{w}}_{ik}^{\chi} - \mathbf{f}_i \cdot \boldsymbol{\xi}_i^{y}. \tag{32}$$

Note that if the Roe matrices are written in Jacobian form, namely,

$$\tilde{\mathsf{A}}_{ik}^{\omega} = \mathbf{A}(\tilde{\mathsf{u}}) \cdot \boldsymbol{\omega},$$

where $\mathbf{A}(\mathsf{u}) = (\mathsf{A}_x(\mathsf{u}), \mathsf{A}_y(\mathsf{u}))^{\mathrm{T}} \in (\mathbb{R}^4 \times \mathbb{R}^4) \times \mathbb{R}^2$, with $\mathsf{A}_x, \mathsf{A}_y \in \mathbb{R}^4 \times \mathbb{R}^4$, is the Jacobian matrix of the flux function $\mathbf{f}(\mathsf{u})$, namely $\mathbf{A}(\mathsf{u}) = \partial \mathbf{f}(\mathsf{u})/\partial \mathsf{u}$, then the property of rotational invariance of the Euler equations can be used to show that the Roe intermediate state $\tilde{\mathsf{u}}$ is a function of the two states u_i and u_k only, namely, it is independent from the chosen direction vector $\boldsymbol{\omega}$, see e.g. [16, p. 321]. Therefore, the three Roe matrices introduced so far share one and the same intermediate state, that is,

$$\tilde{\mathsf{A}}_{ik}^{\eta} = \mathbf{A}(\tilde{\mathsf{u}}) \cdot \boldsymbol{\eta}_{ik}^{y}, \quad \tilde{\mathsf{A}}_{ik}^{\hat{y}} = \mathbf{A}(\tilde{\mathsf{u}}) \cdot \hat{\boldsymbol{y}} \quad \text{and} \quad \tilde{\mathsf{A}}_{ik}^{\chi} = \mathbf{A}(\tilde{\mathsf{u}}) \cdot \boldsymbol{\chi}_{ik}^{y},$$

and the intermediate state $\tilde{\mathsf{u}} = \tilde{\mathsf{u}}(\mathsf{u}_i, \mathsf{u}_k)$ can be computed only once for a given node-pair. The above observation can result in a significant reduction of the computational requirements, especially if non-ideal thermodynamic models are to be considered, as it is the case for example in dense gas flow or chemically reacting flow computations. This property holds also for quasi-Jacobian expressions of the Roe matrix [27,28].

4.3. Time integration

A fully discrete approximation to (19) in now obtained by discretizing the time derivative of the nodal value of the unknown. To this purpose, the high-resolution scheme (32) is recast in the following compact form:

$$L_i^y \frac{\mathrm{d}\mathsf{u}_i}{\mathrm{d}t} = \mathscr{R}_i(\mathsf{u}) = \mathscr{R}_i^{\mathrm{A}}(\mathsf{u}) + \mathscr{R}_i^{\mathrm{S}}(\mathsf{u}),$$

where the source terms are now considered and where

$$\mathscr{R}_i^{\mathrm{A}}(\mathsf{u}) = -\frac{1}{2} \sum_{k \in \mathscr{K}_{i,\neq}} [(\mathbf{f}_i + \mathbf{f}_k) \cdot \boldsymbol{\eta}_{ik}^{y} + \tilde{\mathsf{R}}_{ik}^{\eta} |\tilde{\Lambda}_{ik}^{\eta}| (\tilde{\mathsf{w}}_{ik}^{\eta} - \tilde{\mathsf{v}}_{ik}^{\eta}) - M_{ik} \tilde{\mathsf{R}}_{ik}^{\hat{y}} \tilde{\Lambda}_{ik}^{\hat{y}} \tilde{\mathsf{w}}_{ik}^{\hat{y}}] - \frac{1}{2} \sum_{k \in \mathscr{K}_{i,\neq}^{\partial}} \tilde{\mathsf{R}}_{ik}^{\chi} \tilde{\Lambda}_{ik}^{\chi} \tilde{\mathsf{w}}_{ik}^{\chi} - \mathbf{f}_i \cdot \boldsymbol{\xi}_i^{y},$$

$$\mathscr{R}_i^{\mathrm{S}}(\mathsf{u}) = \sum_{k \in \mathscr{K}_i} M_{ik} \mathsf{s}_k = \sum_{k \in \mathscr{K}_i} M_{ik} (0, 0, \Pi(\mathsf{u}_k), 0)^{\mathrm{T}}.$$

In the following, the expression of the fully discrete equations is given, considering both unsteady and steady flow problems. Note that for the scalar conservation law considered in Section 2, no source terms are present.

4.3.1. Unsteady flows

Time integration for unsteady flows is performed via the well-known operator splitting technique of Strang [31], that introduces a second-order splitting error in time. The time integration from the discrete time level n to time level $n+1$ is therefore performed as follows:

$$\text{Substep 1}: \quad L_i^y \frac{\hat{\mathsf{u}}_i^{n+1/2} - \mathsf{u}_i^n}{\Delta t/2} = \mathscr{R}_i^{\mathrm{S}}(\mathsf{u}^n),$$

$$\text{Substep 2}: \quad L_i^y \frac{\hat{\mathsf{u}}_i^{n+1} - \hat{\mathsf{u}}_i^{n+1/2}}{\Delta t} = \mathscr{R}_i^{\mathrm{A}}(\hat{\mathsf{u}}^{n+1/2}),$$

$$\text{Substep 3}: \quad L_i^y \frac{\mathsf{u}_i^{n+1} - \hat{\mathsf{u}}_i^{n+1}}{\Delta t/2} = \mathscr{R}_i^{\mathrm{S}}(\hat{\mathsf{u}}^{n+1}),$$

where $\Delta t = t^{n+1} - t^n$, with t^{n+1} and t^n are the times at level n and $n+1$, respectively, and where at each substep a forward Euler differencing has been employed. More accurate time integration techniques can be considered at each substep; in the present computations, the three-step total variation bounded scheme of Shu [32] has been used to increase the stability limit of the scheme. Note that the first and the last substeps can be gathered together to reduce the number of evaluations of the source term, in accordance with the well known staggered integration procedure proposed by Strang. The above time integration scheme is subjected to stability conditions, namely, the time step size is limited by the maximum allowable Courant–Friedrichs–Lewy (CFL) number [24]. Following Giles [33], the time step is computed as

$$\Delta t = \mathrm{CFL} \min_{i \in \mathscr{K}} \left[\frac{2L_i^y}{\max\limits_{p=1,\ldots,4} |\tilde{\lambda}_{ik,p}^{\boldsymbol{\eta}}|} \right].$$

In all the unsteady flows computations, $\mathrm{CFL} \leqslant 1$.

4.3.2. Steady flows

For steady flows computations, an implicit backward Euler has been used to integrate in pseudo-time to the steady state solutions, namely

$$L_i^y \frac{\Delta \mathsf{u}_i^n}{\Delta t} = \mathscr{R}_i(\mathsf{u}^{n+1}),$$

where $\Delta \mathsf{u}^n = \mathsf{u}^{n+1} - \mathsf{u}^n$, because of its higher stability limit with respect to the explicit scheme presented in the previous section. Note that for a linear problem, the backward Euler scheme is unconditionally stable. The solution is assumed to have reached steady state when the L_2 norm of the residual vector is 10^{-12} that of the initial residual at time $t = 0$. The residual at time t^{n+1} is approximated via a Taylor expansion centered in t^n as follows:

$$\mathscr{R}_i(\mathsf{u}^{n+1}) \simeq \mathscr{R}_i(\mathsf{u}^n) + \frac{\partial \mathscr{R}_i(\mathsf{u}^n)}{\partial \mathsf{u}^n} \Delta \mathsf{u}^n.$$

The Jacobian of the residual is further approximated by considering the first-order upwind scheme contribution only, to give,

$$\frac{\partial \mathscr{R}_i(\mathsf{u}^n)}{\partial \mathsf{u}^n} \Delta \mathsf{u}^n \simeq \sum_{k \in \mathscr{K}_i} \frac{\partial \mathscr{R}_i^{\mathrm{I}}(\mathsf{u}^n)}{\partial \mathsf{u}_k^n} \Delta \mathsf{u}_k^n,$$

where the fact that in the first-order finite volume scheme, namely,

$$\mathscr{R}_i^{\mathrm{I}}(\mathsf{u}) = -\sum_{k \in \mathscr{K}_{i,\neq}} \left[\frac{\mathbf{f}_i + \mathbf{f}_k}{2} \cdot \boldsymbol{\eta}_{ik}^y - \frac{1}{2} |\tilde{\mathsf{A}}_{ik}^{\boldsymbol{\eta}}| (\mathsf{u}_k - \mathsf{u}_i) \right] - \mathbf{f}_i \cdot \boldsymbol{\xi}_i^y + L_i \mathsf{s}_i$$

the residual for node i depends only on the solution in i and on the node-pairs having i itself as a node has been accounted for. To summarize, one has

$$\frac{\partial \mathscr{R}_i^{\mathrm{I}}(\mathsf{u}^n)}{\partial \mathsf{u}_i^n} = \frac{\partial B_i(\overline{\mathsf{u}}_i^n)}{\partial \mathsf{u}_i^n} - L_i \frac{\partial s_i}{\partial \mathsf{u}_i} = \left[\mathbf{A}(\overline{\mathsf{u}}_i^n) \cdot \boldsymbol{\xi}_i^y \right] \frac{\partial \overline{\mathsf{u}}_i^n}{\partial \mathsf{u}_i^n} - L_i \frac{\partial \Pi(\mathsf{u}_i)}{\partial \mathsf{u}_i} \hat{\mathsf{y}},$$

$$\frac{\partial \mathscr{R}_i^{\mathrm{I}}(\mathsf{u}^n)}{\partial \mathsf{u}_k^n} \simeq -\frac{1}{2} \left[\mathbf{A}(\mathsf{u}_k^n) \cdot \boldsymbol{\eta}_{ik}^y - |\tilde{\mathsf{A}}_{ik}^{\boldsymbol{\eta}}| \right],$$

$$\frac{\partial \mathscr{R}_k^{\mathrm{I}}(\mathsf{u}^n)}{\partial \mathsf{u}_i^n} \simeq \frac{1}{2} \left[\mathbf{A}(\mathsf{u}_i^n) \cdot \boldsymbol{\eta}_{ik}^y + |\tilde{\mathsf{A}}_{ik}^{\boldsymbol{\eta}}| \right],$$

where the Roe matrix $\mathsf{A}^{\boldsymbol{\eta}}_{ik}$ is evaluated at time level t^n and it is assumed not to depend on u_i and u_k, to reduce the computational cost of the evaluation of the Jacobian matrix. Note that all the approximations introduced in the evaluation of the Jacobian matrix of the residual do not affect the final steady state solution, since the left-hand side vanishes as $\Delta\mathsf{u}^n_i \to 0$. The fully discrete scheme finally reads

$$\left[\frac{L^y_i}{\Delta t} - [\mathbf{A}(\overline{\mathsf{u}}^n_i)\cdot\boldsymbol{\xi}^y_i]\frac{\partial\overline{\mathsf{u}}^n_i}{\partial\mathsf{u}^n_i} - L_i\frac{\partial\Pi^n_i}{\partial\mathsf{u}^n_i}\hat{\mathsf{y}}\right]\Delta\mathsf{u}^n_i + \sum_{k\in\mathscr{K}_{i,\neq}}\frac{1}{2}[\mathbf{A}(\mathsf{u}^n_k)\cdot\boldsymbol{\eta}^y_{ik} - |\tilde{\mathsf{A}}^{\boldsymbol{\eta}}_{ik}|]\Delta\mathsf{u}^n_k = \mathscr{R}_i(\mathsf{u}^n).$$

The resulting linear system is solved by means of the direct linear solver for sparse matrices UMFPack [34]. A local time-stepping technique [33] has been adopted in the computations, where the time step at each node is computed as

$$(\Delta t)_i = \mathrm{CFL}\left[\frac{2L^y_i}{\max\limits_{p=1,\ldots,4}|\tilde{\lambda}^{\boldsymbol{\eta}}_{ik,p}|}\right].$$

The CFL is computed via a function that is inversely proportional to the L_2 norms of the residual and it is allowed to vary from a minimum of 0.5 to a maximum of 10^9 at convergence, where linear behavior is expected.

5. Numerical results

The proposed numerical scheme is now applied to scalar advection problems (Section 5.1) and to compressible inviscid axisymmetric flows of ideal gases. The capability of the numerical method in computing unsteady flows is tested against experimental results for a shock-tube problem in Section 5.2. Steady state computations are performed for under-expanded nozzle flows (Section 5.3) and results are compared with available experimental data.

5.1. Scalar advection

The TVD scheme presented in the previous section is now applied to the computation of linear advection problems under the assumption of axial symmetry. The model equation reads

$$\frac{\partial u}{\partial t} + \boldsymbol{a}(\boldsymbol{x})\cdot\nabla u = 0,$$

with $\boldsymbol{a}\in\mathbb{R}^2$ advection velocity. The equation above can be recast in the conservative form $\partial u/\partial t + \nabla\cdot\boldsymbol{f} = 0$ by setting $\boldsymbol{f} = \boldsymbol{f}(u,\boldsymbol{x}) = \boldsymbol{a}(\boldsymbol{x})u$, provided that the axisymmetric advection field is solenoidal, i.e., $\nabla\cdot\boldsymbol{a}\equiv 0, \forall\boldsymbol{x}\in\Omega$. This is indeed the case of the advection field considered in the numerical experiments, namely, the source flow of an incompressible fluid originating at $(0,0)$. The advection field is endowed with spherical symmetry; the velocity vector is therefore parallel to the radii from $(0,0)$ and its module depends only on the distance R, $R=\sqrt{x^2+y^2}$, from the origin, namely, $|\boldsymbol{a}| = Q/(4\pi\overline{\rho}R^2)$, with Q (constant) mass flow per unit time and $\overline{\rho}$ (constant) fluid density. The constant Q is taken as $4\pi\overline{\rho}$, so that $|\boldsymbol{a}| = 1$ at $R=1$, see Fig. 6. Therefore, the velocity vector reads $\boldsymbol{a} = (|\boldsymbol{a}|\cos\psi, |\boldsymbol{a}|\sin\psi)$, with $\psi = \operatorname{atan}(y/x)$, or

$$\boldsymbol{a}(x,y) = \frac{(x,y)^{\mathrm{T}}}{(x^2+y^2)^{3/2}}.$$

The exact solution to the present advection problem is readily obtained from the method of characteristics (characteristic curves are straight lines from $(0,0)$ here) as

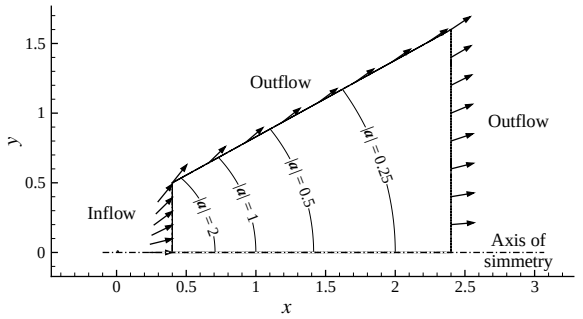

Fig. 6. Geometry and advection field for the numerical experiments. The inflow and outflow boundaries are indicated together with isolines of the module $|\boldsymbol{a}|$ of the advection velocity. The length of the arrow is not proportional to the local speed.

$$u(x,y,t) = u_0\left(x\sqrt{1-\frac{3t}{(x^2+y^2)^{3/2}}}, y\sqrt{1-\frac{3t}{(x^2+y^2)^{3/2}}}\right)^{\mathrm{T}},$$

where u_0 is the initial condition at time $t = 0$, $u(\boldsymbol{x},0) = u_0(\boldsymbol{x})$.

Two different initial conditions have been considered for the domain depicted in Fig. 6. To assess the order of accuracy of the integration scheme, a smooth initial profile is considered first, namely,

$$u_0(\boldsymbol{x}) = \begin{cases} [1+\cos(2\pi|\boldsymbol{x}-\boldsymbol{x}_c|)][1+\cos(2\pi|\boldsymbol{x}-\boldsymbol{x}_c|)] & \text{for } |\boldsymbol{x}-\boldsymbol{x}_c| \leqslant \sigma, \\ 0 & \text{for } |\boldsymbol{x}-\boldsymbol{x}_c| > \sigma, \end{cases}$$

which corresponds to a "cosine-hill" profile of radius $\sigma = 0.5$ centered in $\boldsymbol{x}_c = (1,0)$. Integration in time is performed from $t_0 = 0$ to a final time $t_f = 7/3$; correspondingly, the center of the cosine-hill profile moves from $(1,0)$ to $(2,0)$, see Fig. 7 (bottom).

In Figs. 7 and 8 the numerical results for an smooth initial profile are compared to the exact solution for grids of different size, see Table 1. The integration in time has been performed by means of a third-order Runge–Kutta scheme. All grids are unstructured grids of triangles with uniform size h (see Fig. 7, top). Note

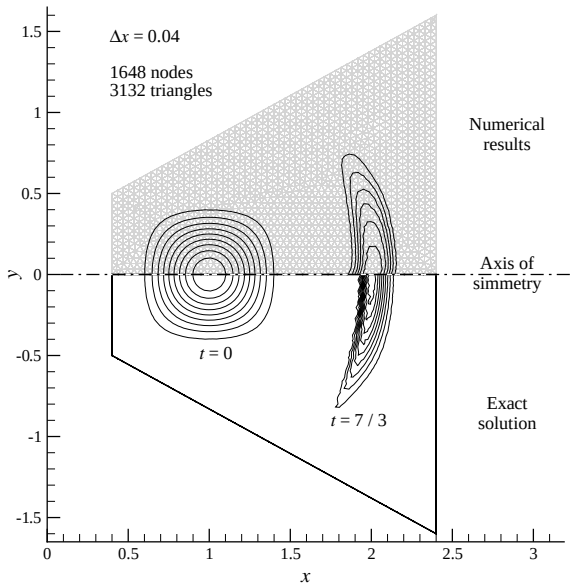

Fig. 7. Numerical results for smooth initial data on the coarsest grid (top). The isolines represent $\Delta u = 0.1$. The exact solution, shown in the lower part of the plot ($y < 0$), is interpolated on the same grid. Note the time lagging in the numerical solutions due to phase errors.

Table 1
Summary of numerical results for smooth initial data and for different grids

h	Nodes	Elements	$\min u_h$	$\max u_h$	Err	p
0.04	1648	3132	-5.0289×10^{-13}	0.67741	0.35958	–
0.02	6336	12,348	-5.8297×10^{-13}	0.83782	0.18898	0.92808
0.01	24,762	48,881	-8.9109×10^{-13}	0.92887	0.08225	1.20001

Err is the relative error in the L_2 norm, namely, $\mathrm{Err} = \|u_h - u\|_2/\|u\|_2$, with u_h and u numerical and exact solutions, respectively, at time $t = 7/3$; p is the order of convergence, namely, $p = \log(\mathrm{Err}_1/\mathrm{Err}_2)/\log(h_1/h_2)$, with the subscripts indicating two different grids.

that the circular initial profile is severely stretched while propagating due to the strong difference in the velocity magnitude, which varies from $|\boldsymbol{a}(R=1)| = 1$ to $|\boldsymbol{a}(R=2)| = 1/8 = 0.125$. The above can be appreciated in Fig. 8, where the trace of the solution on the axis of symmetry is shown for both the exact and the numerical solutions computed on three grids of different size. The length of the interval in which the solution is different from zero is one at time $t = 0$ and equal to $(\sqrt[3]{59} - \sqrt[3]{33})/2 \simeq 0.343$ at time $t = 7/3$, namely, it is about 34% of its initial value.

The solution is fairly well captured already on the coarser grid (cf. Fig. 7) and the numerical solution converges to the exact one as the grid is refined, see Fig. 8, with no spurious oscillations, as it can be appreciated from Table 1, where the minimum and maximum values of the numerical solution u_h are given for different grid resolutions, together with the L_2 norm of the error, namely, $\mathrm{Err} = \|u_h - u\|_2/\|u\|_2$, with u_h and u numerical and exact solutions, respectively. Note that the order p of accuracy in space is that expected from TVD theory ($1 < p < 2$), though the use of the TVD stabilization technique to prevent the appearance of spurious oscillations significantly reduces the overall accuracy of the scheme with respect to standard Lax–Wendroff [35] or Taylor–Galerkin [36] approaches or to essentially non-oscillatory (ENO) [37] or weighted ENO [38] schemes ($p \geqslant 2$). Thanks to the FE/FV relation demonstrated here, the inclusion of the above high-order scheme can be done in a straightforward manner, depending on the discrete framework, be it the FV or the FE discretization, in which those schemes have been derived. Further work is therefore to be devoted to the development of such accurate schemes for axisymmetric problems.

In Figs. 9 and 10 the numerical results for a discontinuous initial profile are compared to the exact solution for grids of different size. The initial solution is

$$u_0(\boldsymbol{x}) = \begin{cases} 1 & \text{for } |\boldsymbol{x} - \boldsymbol{x}_c| \leqslant \sigma, \\ 0 & \text{for } |\boldsymbol{x} - \boldsymbol{x}_c| > \sigma, \end{cases}$$

namely, the solution is everywhere equal to zero but for a circular region of radius $\sigma = 0.5$ centered in $\boldsymbol{x}_c = (1,0)$. As in the smooth case, the solution is fairly well captured already on the coarser grid (cf. Fig. 9) and the numerical solution converges to the exact one as the grid is refined, see Fig. 10, with no spu-

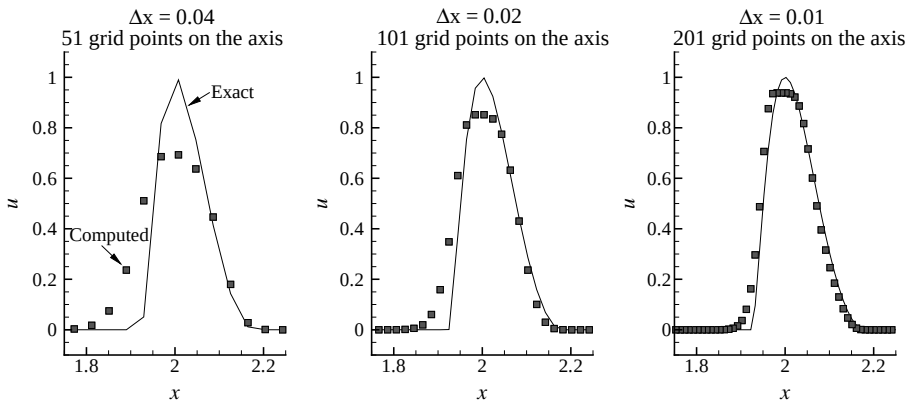

Fig. 8. Solution along the axis of symmetry for three different grid resolutions and smooth initial data. The exact solution is interpolated on each grid.

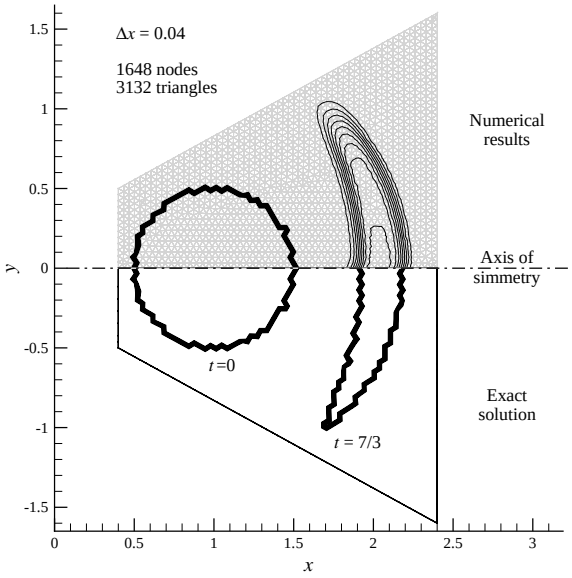

Fig. 9. Numerical simulation results for discontinuous initial data on the coarsest grid. Each isoline represents $\Delta u = 0.1$. The exact solution is interpolated on the same grid and it is represented in the lower part of the plot.

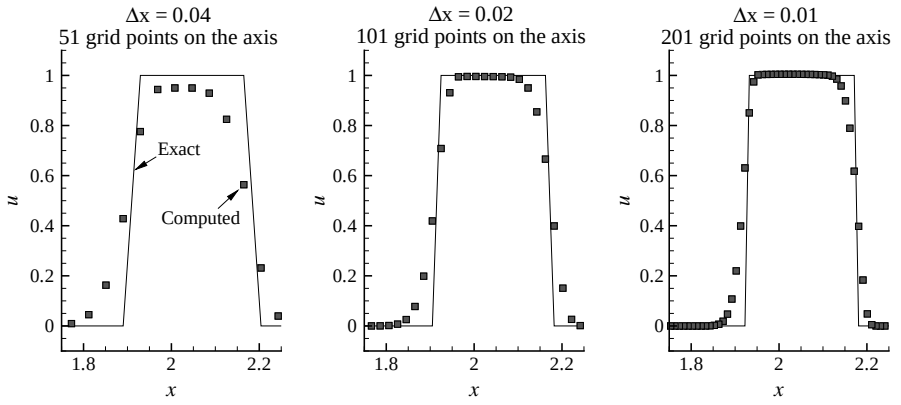

Fig. 10. Solution along the axis of symmetry for three different grid resolutions and discontinuous initial data. The exact solution is represented after interpolation on the three grids.

rious oscillations, thus demonstrating the capability of the present scheme to deal with discontinuous solutions.

5.2. Unsteady shock-tube flows

The imperfect burst of a shock-tube diaphragm may introduce non-negligible multidimensional perturbations in the flowfield that can significant differ from the ideally one-dimensional shock-tube problem, under both qualitative and quantitative point of view [39–43]. To investigate the suitability of the proposed solution technique in the computations of this kind of flows, the results presented in [43], referring to an axisymmetric partial burst of the diaphragm in an existing shock-tube facility, are now compared to numerical simulations.

The shock-tube used in the experimental trials has a cross-sectional circular area with diameter $D = 80$ mm. The high-pressure section is 1500 mm long and it is separated from the low-pressure section (5000 mm long and open to the ambient pressure) by means of a plastic diaphragm. An overpressure of about 1 atm

is maintained in the high-pressure section; the gas is assumed to be at the same temperature in both the high- and low-pressure sections of the tube. Pressure probes are positioned along the tube axis at different axial distances from the diaphragm to measure the total pressure of the incident flow. The experimental facility is intended to produce a normal shock wave propagating towards the low-pressure section of the shock-tube, to be used as the reference signal for the dynamic calibration of fast response pressure probes. High-speed camera recordings and examinations of the shock-tube diaphragm after the experimental trials revealed that the diaphragm did not open completely during the tests, see Fig. 11. An (almost) axisymmetric burst of the diaphragm was observed and resulted in major disturbances in the flowfield. From camera recordings, the diaphragm opening time was estimated to be of about 400 μs. For the details of the experimental setup and a discussions of the results, the reader is referred to [43].

The axisymmetric flowfield is now studied by assuming an instantaneous though incomplete burst of the shock-tube diaphragm. Correspondingly, the initial conditions for the simulations are that of the well-known one-dimensional shock-tube problem, with two constant states, namely, the high-pressure and low-pressure states, in the two corresponding sections of the shock-tube initially separated by the diaphragm. The gas is air in dilute, namely, ideal gas conditions and the effect of viscosity and thermal conductivity are assumed to be negligible.

In Fig. 12, isobars (top) and isophycnics (bottom) of the simulated shock-tube experiments are shown at time $t = 43$ μs. Note that the unopened portion of the diaphragm is assumed to retain its original position and shape. The ratio P_4/P_1 of the pressure P_4 and P_1 in the high-pressure and low-pressure section, respectively, is 2.068. Consistent with the experiment, the diameter d of the open (circular) section is taken as 48 mm, or $d/D = 0.6$.

When the diaphragm is removed at time $t = 0$, a rarefaction wave moving towards the high-pressure section of the shock tube is formed; a shock wave and a contact discontinuity start moving towards the low-pressure section. These waves are planar and normal to the shock tube axis with intensity equal to their one-dimensional counterparts. At time $t = 43$ μs, shortly after leaving the diaphragm section, the shock wave partially diffracts to form an annular shock wave, indicated in Fig. 12 as diffracted shock. A portion of the initial shock wave remains unchanged and moves as a planar shock, normal to the axis of the shock-tube. The expansion at the diaphragm's edge results in a rarefaction wave moving towards the shock-tube axis. The rarefaction wave is faster than the leading normal shock and eventually collides with the shock itself. Flow separation occurs at the diaphragm's edge and a slipstream is formed and rolls up into an annular vortex; a well-known process already observed in two-dimensional shock wave diffraction [44]. At higher times (not shown), the diffracted portions of the shock and rarefaction waves are reflected by the tube walls and at the tube axis. Moreover, the reflected shock interacts with the vortex and the contact surface, resulting in additional waves reflecting along the shock tube.

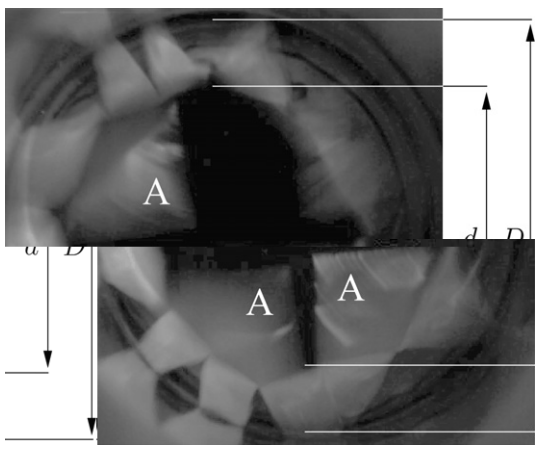

Fig. 11. Diaphragm bursting process. An incomplete and nearly axisymmetric petaling of the plastic layer is observed. D is the diameter of the diaphragm, namely, the inner diameter of the shock tube; d is the diameter of the opened portion of the diaphragm. Three out of the four pre-cut aluminum plates are visible on the high-pressure side of the diaphragm, marked with the letter A. The plates are very flexible and they do not contribute to blockage.

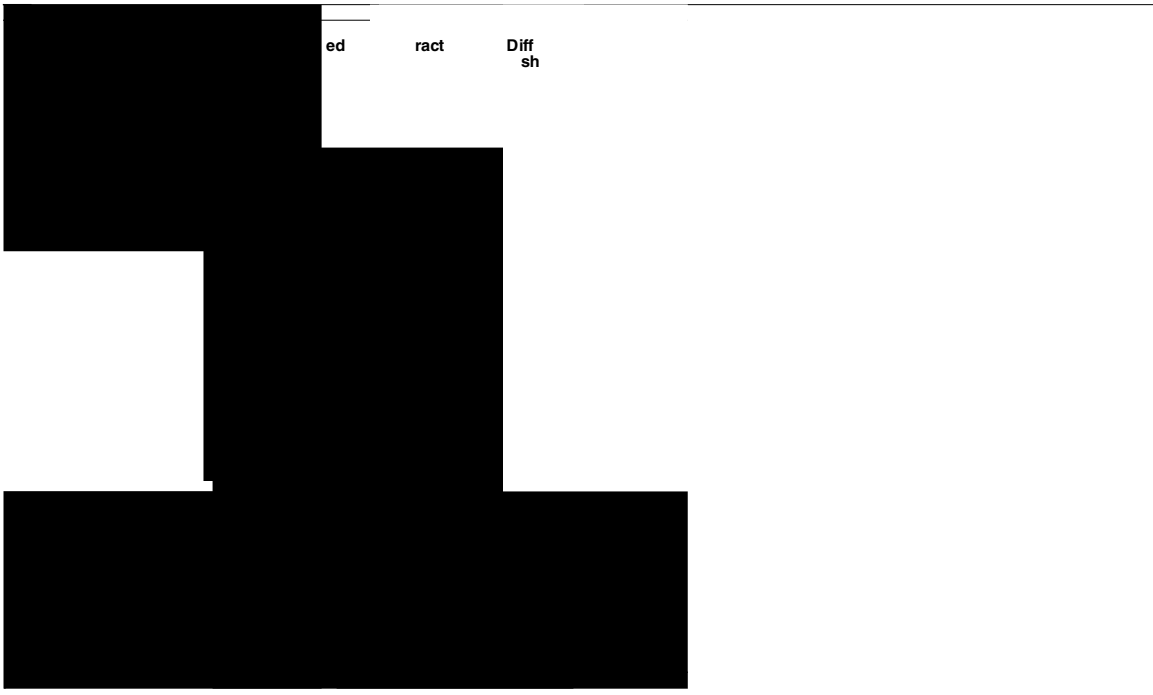

Note that the characteristic time scale, namely, $t = 43$ μs, associated with the first reflection is one order of magnitude lower than the estimated diaphragm opening time of 400 μs, thus making the assumption of a negligible opening time unrealistic. It is however true that all the details of the initial diffraction/reflection process are lost at large distances from the diaphragm, where a single shock front is eventually formed. The above can be appreciated in Fig. 13, where numerical results are compared with total pressure measurements along the

shock tube axis at a distance from the diaphragm of 970 mm (12.125D), for $d/D = 0.7$ and $P_4/P_1 = 1.857$. Differences between the experimental data and the numerical results are limited to a time interval of about 400 μs, and they become irrelevant for measurement stations located further away from the diaphragm. Despite the different diaphragm opening mechanisms considered in the simulations, the observed flowfield at measurement stations sufficiently far away from the diaphragm is therefore correctly captured by the numerical model.

5.3. Steady under-expanded nozzle flows

Steady state simulations of the compressible flow outside an under-expanded nozzle, namely, a gasdynamic nozzle in which the pressure P_e at the exit section or discharge pressure is higher than the ambient pressure P_a, are now performed. The nozzle is connected to a reservoir at constant pressure P_r, in which gaseous nitrogen is at rest. Isentropic flow is assumed from the reservoir to the nozzle inlet. Experimental data are taken from [45], where Schlieren images of the external flowfield and total pressure measurements along the axis of symmetry are presented. In the computations, geometry 1.5C of [45] has been considered, see Fig. 14.

The main feature of the flowfield is depicted in Fig. 15, with the appearance of the well-known barrel shock wave, topped by a Mach disk, namely, a shock wave with a circular surface normal to the axis of symmetry. The mechanism that is responsible for the formation of such a complicated wavefield is as follows. Past the nozzle, the flow undergoes an expansion to the ambient pressure. The expansion fan reflects at the axis of symmetry back to the constant pressure (ambient pressure) boundary, where it is reflected as a compression fan. Compression waves eventually coalesce into a curved shock (barrel shock), that reflects at the axis of symmetry with a lambda pattern (barrel shock-Mach disk-reflected shock). For a detailed description of the flow features, the reader is referred to [46].

The computations were performed on an unstructured grid made of 8482 triangular elements (4386 nodes). The computational domain includes the nozzle and extends from the nozzle exit up to $x/D_e = 10$ and $y/D_e = 2.5$ in the axial and radial directions, respectively. Constant pressure boundary conditions are enforced at numerical boundaries. In particular, a constant pressure boundary condition was imposed so that the gas pressure eventually reaches the value of the ambient pressure P_a. The subsonic inflow boundary conditions are enforced in terms of inlet density and pressure to ensure that the flow total pressure at the inlet is equal to its reservoir value P_r, where the gas velocity is zero, in accordance with the isentropic flow assumption.

Results of the simulations are shown in Fig. 16, where Schlieren images of the computed outer flows are compared with experiments. All the relevant features are well captured by the numerical scheme. In

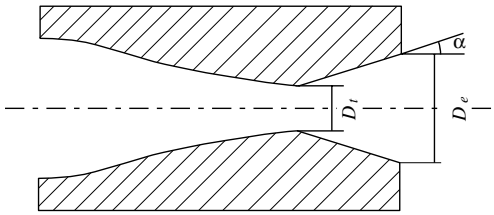

Fig. 14. Geometry of the nozzle 1.5C from [45], with $\alpha = 7.5°$, $D_t = 6$ mm (throat section diameter) and $D_e = 6.5$ mm (exit section diameter).

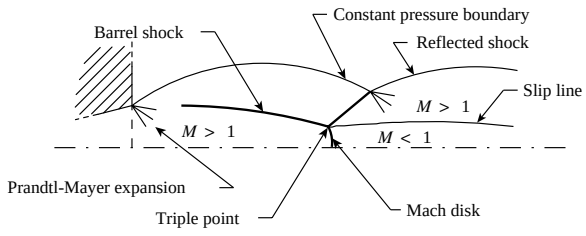

Fig. 15. Representative flow features and wave structures for an under-expanded nozzle flow expanding in still air.

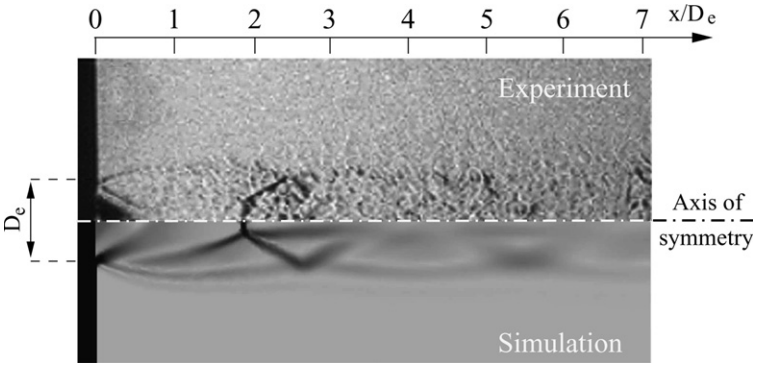

Fig. 16. Experimental (top, from [45]) and numerical (bottom) Schlieren images of the flow expansions outside the nozzle, for $P_r/P_a = 8$. The main features of the wavefield are clearly visible (cf. Fig. 15) and well captured by the numerical scheme. D_e is the diameter of the nozzle exit section.

Fig. 17, total pressure measurements along the axis of symmetry are compared with experimental results for the case $P_r/P_a = 10$. Experimental results are taken from [45]. The Pitot total pressure in Fig. 17 is computed according to the following relations:

$$\frac{P^t}{P} = \begin{cases} \left(\frac{\gamma-1}{2}M^2\right)^{\frac{\gamma}{\gamma-1}}\left(\frac{2\gamma}{\gamma-1}M^2 - 1\right)^{-\frac{1}{\gamma-1}} & \text{if } M > 1, \\ \left(\frac{\gamma-1}{2}M^2\right)^{\frac{\gamma}{\gamma-1}} & \text{if } M < 1 \end{cases} \tag{33}$$

to account for the formation of a bow shock in front of the probe head in the case of supersonic flow measurements. The total pressure jump across the bow shock is computed according to standard formulas for normal shock waves. A very good agreement between experimental and numerical results is found up to the Mach disk location, whose position is well captured in the simulations. As pointed out in [45], downwind the Mach disk, viscosity plays a major role in determining the momentum flux across the slip line (cf. Fig. 15), separating the subsonic region behind the normal shock wave (the Mach disk) and the outer supersonic flow, a detail that cannot be captured under the inviscid approximation considered here.

To further investigate the capability of the scheme to reproduce the inviscid features of the flowfield, sonic nozzle flow expanding in still air are now considered. Experimental results are taken from [47], where a

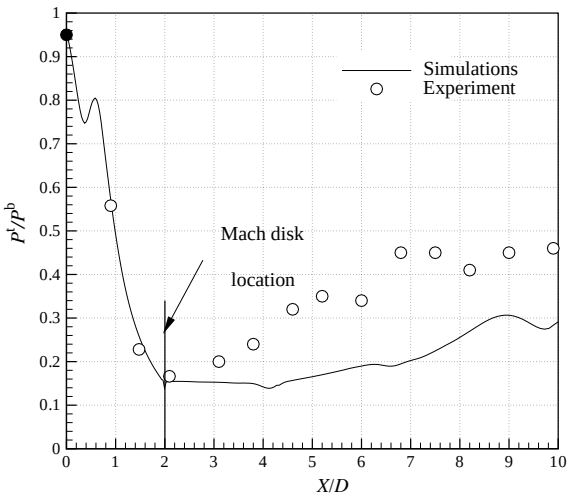

Fig. 17. Total pressure measurements from [45] along the axis of symmetry against numerical results for nozzle 1.5C with $P_r/P_a = 10$. The Pitot total pressure is computed according to relations (33).

description of the experimental set-up is also given. The geometry of the nozzle is shown in Fig. 18a. The nozzle is connected to a reservoir at constant pressure P_r where the fluid is at rest. Isentropic flow is assumed to occur between the reservoir and the nozzle inlet, where the flow is subsonic. The nozzle inlet section is circular with a diameter D_i of 50.8 mm. The gas is accelerated to sonic conditions at the throat section, namely, the nozzle exit section (diameter $D_e = 12.7$ mm). The quantities considered for the comparisons are the axial distance L_m between the nozzle exit and the Mach disk and the Mach disk diameter D_m, see Fig. 18b. Addy [47] showed that L_m and D_m are almost independent on the convergent angle β in Fig. 18a and that they are nicely approximated by the following empirical relations:

$$\frac{L_m}{D_e} = 0.65\sqrt{\frac{P_r}{P_a}} \quad \text{and} \quad \frac{D_m}{D_e} = 0.31\sqrt{\frac{P_r}{P_a} - 5}. \tag{34}$$

In Fig. 19, experimental data from [47] for the dimensionless characteristic length L_m/D_e and D_m/D_e are compared to numerical results for different values of the reservoir to ambient pressure ratio P_r/P_a. All simulations were performed on the same grid made of 6566 nodes and 12,772 triangular elements. Boundary conditions are imposed as in the previous section.

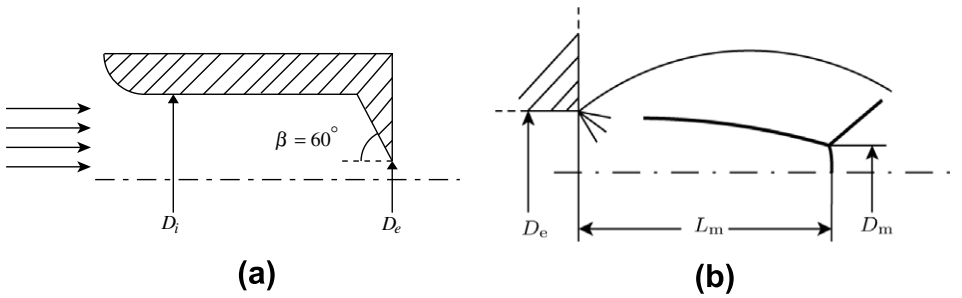

Fig. 18. Geometry (a) and definitions of significant flow features (b) for the sonic nozzle experiments of Addy [47]. $D_i = 50.8$ mm and $D_e = 12.7$ mm are the inlet and exit cross-section diameter of the nozzle; L_m is the axial distance between the nozzle exit and the Mach disk, D_m is the diameter of the Mach disk.

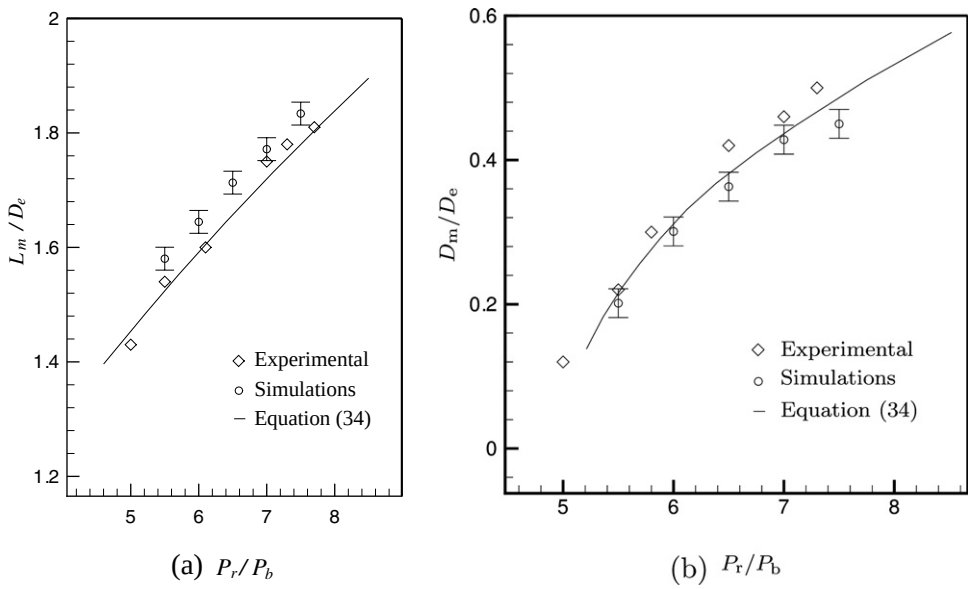

Fig. 19. Experimental and numerical results for the sonic nozzle case. Dimensionless Mach disk position L_e/D_e and diameter D_m/D_e, with D_e diameter of the nozzle exit section, for different values of the reservoir to ambient pressure ratio. The empirical correlations (34) are also shown. Error bars in the numerical results represent the uncertainty related to the determination of the correct shock position in shock-capturing computations, the shock being spread across three/four computational elements.

Numerical results are found to agree fairly well with the experimental data and with the empirical relations (34). Error bars have been included in the representation of the numerical results. In fact, in the present shock-capturing scheme the Mach disk is not represented by a flow discontinuity of zero thickness, but instead it is spread across three/four computational elements.

6. Conclusions

The node-pair finite element approximation to the Euler equations for axisymmetric flows, including swirling flows, has been derived. By mimicking the demonstration given by Selmin [3] for Cartesian coordinates, a relation was found linking the node-pair finite element representation of the conservation law to its finite volume counterpart, opening the way to the development of hybrid finite element/volume schemes in the TVD framework. The limiting procedure in the TVD scheme was extended to take into account higher-order finite element terms, including the node-pair boundary term that was dismissed by Selmin [3]. The proposed numerical technique allows for a straightforward implementation in existing node-pair finite volume computer codes written for Cartesian coordinates. Moreover, the equivalence of the FV and FE demonstrated here allows for the inclusion of other stabilization techniques for the Euler equations derived in the FV framework, such as for example essentially non-oscillatory (ENO) schemes.

Thanks to the FV/FE equivalence demonstrated here, the FE discretization of the viscous terms can be easily included in a straightforward manner. The study of viscous flows will be undertaken in future developments of the scheme. The possibility of switching between FE and FV schemes proved already to be useful here in the treatment of the source terms, where a second-order FE representation of the source terms has been easily attained by means of a FE reinterpolation of the data, instead of the standard, first order, piece-wise constant FV representation.

The correct treatment of the axis of symmetry is a built-in of the proposed method, thanks to the vanishing of the boundary metric quantities, and hence of the boundary integrated flux, at the axis. No special treatment or numerical artifices are required to be used at the axis of symmetry.

Numerical results have been presented for scalar advection in a source flow, including both continuous and discontinuous initial data and demonstrate the correctness of the proposed approach. Within the limits of the underlying inviscid model for compressible flows, the present scheme was found to be also capable of correctly representing both steady and unsteady axisymmetric flows of compressible fluids. The numerical results were found to be in good agreement with available experimental data for unsteady shock-tube flows and for the steady flow at the exit of under-expanded and sonic nozzles.

Further work is underway to extend the proposed methodology to three-dimensional problems in cylindrical coordinates and to spherically symmetric viscous flows.

Acknowledgment

The authors thank Federico Muccioli for his help in the development of the computer code and for running all the steady state simulations.

Appendix A. Node-pair finite element for a scalar conservation law

In this appendix, the following two identities are demonstrated, namely

$$\sum_{k\in\mathscr{K}_i} \boldsymbol{f}_k \cdot \int_{\Omega_{ik}} y\phi_k \nabla\phi_i = -\frac{1}{2}\sum_{k\in\mathscr{K}_{i,\neq}} [(\boldsymbol{f}_i+\boldsymbol{f}_k)\cdot\boldsymbol{\eta}^y_{ik} - \hat{\boldsymbol{y}}\cdot(\boldsymbol{f}_k-\boldsymbol{f}_i)M_{ik}] + \frac{1}{2}\sum_{k\in\mathscr{K}^{\partial}_{i,\neq}} (\boldsymbol{f}_k-\boldsymbol{f}_i)\cdot\boldsymbol{\chi}^y_{ik}, \tag{A.1}$$

and

$$\sum_{k\in\mathscr{K}^{\partial}_i} \boldsymbol{f}_k \cdot \int_{\partial\Omega^{\partial}_{ik}} y\phi_i\phi_k \boldsymbol{n} = \sum_{k\in\mathscr{K}^{\partial}_{i,\neq}} (\boldsymbol{f}_k-\boldsymbol{f}_i)\cdot\boldsymbol{\chi}^y_{ik} + \boldsymbol{f}_i\cdot\boldsymbol{\xi}^y_i, \tag{A.2}$$

which together allow to recast the discrete Galerkin equation (8) into its node-pair counterpart (9). The integral in the left-hand side of (A.1) is decomposed in elemental contribution as

$$\sum_{k\in\mathscr{K}_i}\boldsymbol{f}_k\cdot\int_{\Omega_{ik}}y\phi_k\boldsymbol{\nabla}\phi_i=\sum_{e\in\mathscr{E}_i}\sum_{k\in\mathscr{K}^e}\boldsymbol{f}_k\cdot\int_{\Omega^e}y\phi_k\boldsymbol{\nabla}\phi_i, \tag{A.3}$$

where $\mathscr{E}_i$ is the set of elements sharing node i, the so-called element bubble of i, and $\mathscr{K}^e$ is the set of nodes of the eth element. Note that $\Omega_i=\bigcup_{e\in\mathscr{E}_i}\Omega^e$. From the gradient theorem, one has

$$\int_{\Omega^e}\boldsymbol{\nabla}(y\phi_i\phi_k)=\int_{\Omega^e}\phi_i\phi_k\hat{\boldsymbol{y}}+\int_{\Omega^e}y\phi_k\boldsymbol{\nabla}\phi_i+\int_{\Omega^e}y\phi_i\boldsymbol{\nabla}\phi_k=\oint_{\partial\Omega^e}y\phi_i\phi_k\boldsymbol{n}, \tag{A.4}$$

and therefore

$$2\int_{\Omega^e}y\phi_k\boldsymbol{\nabla}\phi_i=-\int_{\Omega^e}y(\phi_i\boldsymbol{\nabla}\phi_k-\phi_k\boldsymbol{\nabla}\phi_i)-\int_{\Omega^e}\phi_i\phi_k\hat{\boldsymbol{y}}+\oint_{\partial\Omega^e}y\phi_i\phi_k\boldsymbol{n}.$$

By substituting the relation above into (A.3) and summing up on all elements,

$$\begin{aligned}\sum_{k\in\mathscr{K}_i}\boldsymbol{f}_k\cdot\int_{\Omega_{ik}}y\phi_k\boldsymbol{\nabla}\phi_i&=-\frac{1}{2}\sum_{k\in\mathscr{K}_i}\boldsymbol{f}_k\cdot\left[\int_{\Omega_{ik}}y(\phi_i\boldsymbol{\nabla}\phi_k-\phi_k\boldsymbol{\nabla}\phi_i)+\int_{\Omega_{ik}}\phi_i\phi_k\hat{\boldsymbol{y}}-\int_{\partial\Omega^\partial_{ik}}y\phi_i\phi_k\boldsymbol{n}\right]\\&=-\frac{1}{2}\sum_{k\in\mathscr{K}_i}\boldsymbol{f}_k\cdot[\boldsymbol{\eta}^y_{ik}+M_{ik}\hat{\boldsymbol{y}}-\boldsymbol{\chi}^y_{ik}],\end{aligned} \tag{A.5}$$

where the metric quantities defined in (10) have been introduced. Note that $\boldsymbol{\chi}^y_{ik}\neq\boldsymbol{0}$ only if nodes i and k belong to the domain boundary $\partial\Omega$, namely, if and only if $i\in\mathscr{K}^\partial$ and $k\in\mathscr{K}^\partial$. On the other hand, by manipulating relation (A.4), one also has

$$\int_{\Omega^e}y(\phi_i\boldsymbol{\nabla}\phi_k-\phi_k\boldsymbol{\nabla}\phi_i)-\int_{\Omega^e}\phi_i\phi_k\hat{\boldsymbol{y}}+\oint_{\partial\Omega^e}y\phi_i\phi_k\boldsymbol{n}=2\int_{\Omega^e}y\phi_i\boldsymbol{\nabla}\phi_k$$

namely, recalling that $\sum_{k\in\mathscr{K}^e}\boldsymbol{\nabla}\phi_k(\boldsymbol{x})\equiv 0\ \forall\boldsymbol{x}\in\Omega^e$,

$$\sum_{k\in\mathscr{K}^e}\left[\int_{\Omega^e}y(\phi_i\boldsymbol{\nabla}\phi_k-\phi_k\boldsymbol{\nabla}\phi_i)-\int_{\Omega^e}\phi_i\phi_k\hat{\boldsymbol{y}}+\oint_{\partial\Omega^e}y\phi_i\phi_k\boldsymbol{n}\right]=\boldsymbol{0}.$$

By summing up for all elements $e\in\mathscr{E}_i$ and recalling the definitions (10) of the metric quantities, one has

$$\sum_{k\in\mathscr{K}_i}[\boldsymbol{\eta}^y_{ik}-M^y_{ik}\hat{\boldsymbol{y}}+\boldsymbol{\chi}^y_{ik}]=\boldsymbol{0}. \tag{A.6}$$

Relation (A.1) is finally obtained by subtracting the above zero quantity multiplied by $\boldsymbol{f}_i$ from (A.5), namely,

$$\sum_{k\in\mathscr{K}_i}\boldsymbol{f}_k\cdot\int_{\Omega_{ik}}y\phi_k\boldsymbol{\nabla}\phi_i=-\frac{1}{2}\sum_{k\in\mathscr{K}_{i,\neq}}[(\boldsymbol{f}_k+\boldsymbol{f}_i)\cdot\boldsymbol{\eta}^y_{ik}-\hat{\boldsymbol{y}}\cdot(\boldsymbol{f}_k-\boldsymbol{f}_i)M^y_{ik}]+\frac{1}{2}\sum_{k\in\mathscr{K}^\partial_{i,\neq}}(\boldsymbol{f}_k-\boldsymbol{f}_i)\cdot\boldsymbol{\chi}^y_{ik}, \tag{A.7}$$

where the boundary terms have been put into evidence and all summations have been limited to node-pair quantities only, since all terms are identically zero for $k=i$.

Considering now the boundary integral (A.2), the contribution pertaining to node i only is first put into evidence, namely,

$$\sum_{k\in\mathscr{K}^\partial_i}\boldsymbol{f}_k\cdot\int_{\partial\Omega^\partial_{ik}}y\phi_i\phi_k\boldsymbol{n}=\sum_{k\in\mathscr{K}^\partial_{i,\neq}}\boldsymbol{f}_k\cdot\int_{\partial\Omega^\partial_{ik}}y\phi_i\phi_k\boldsymbol{n}+\boldsymbol{f}_i\cdot\int_{\partial\Omega^\partial_i}y\phi_i\phi_i\boldsymbol{n}.$$

The quantity

$$\sum_{k\in\mathscr{K}^\partial_{i,\neq}}\boldsymbol{f}_i\cdot\int_{\partial\Omega^\partial_{ik}}y\phi_i\phi_k\boldsymbol{n}$$

is now added and subtracted from the right-hand side to obtain

$$\sum_{k\in\mathscr{K}_i^\partial} \boldsymbol{f}_k \cdot \int_{\partial\Omega_{ik}^\partial} y\phi_i\phi_k \boldsymbol{n} = \sum_{k\in\mathscr{K}_{i,\neq}^\partial} (\boldsymbol{f}_k - \boldsymbol{f}_i) \cdot \int_{\partial\Omega_{ik}^\partial} y\phi_i\phi_k \boldsymbol{n} + \boldsymbol{f}_i \cdot \sum_{k\in\mathscr{K}_i^\partial} \int_{\partial\Omega_i^\partial} y\phi_i\phi_k \boldsymbol{n}.$$

Then, by recalling that $\sum_{k\in\mathscr{K}_i}\phi_k(\boldsymbol{x}) \equiv 1 \ \forall \boldsymbol{x}\in\Omega_i$, one has

$$\sum_{k\in\mathscr{K}_i^\partial} \boldsymbol{f}_k \cdot \int_{\partial\Omega_{ik}^\partial} y\phi_i\phi_k \boldsymbol{n} = \sum_{k\in\mathscr{K}_{i,\neq}^\partial} (\boldsymbol{f}_k - \boldsymbol{f}_i) \cdot \int_{\partial\Omega_{ik}^\partial} y\phi_i\phi_k \boldsymbol{n} + \boldsymbol{f}_i \cdot \int_{\partial\Omega_i^\partial} y\phi_i \boldsymbol{n},$$

namely, from definitions (10), relation (A.2).

Appendix B. Axisymmetric compressible swirling flows

In the present appendix, the Euler equations for compressible axisymmetric flows, including a possibly non-zero tangential velocity (swirling flows), are derived and the possibility of treating swirling flows in the framework of the proposed hybrid FE/FV scheme is discussed.

In three spatial dimensions, the Euler equations describing the flow of a compressible fluid with zero viscosity and zero thermal conductivity read

$$\frac{\partial \mathsf{u}}{\partial t} + \nabla\cdot\mathbf{f}(\mathsf{u}) = 0, \tag{B.1}$$

where $\mathsf{u} = (\rho, \boldsymbol{m}, E^{\mathrm{t}})^{\mathrm{T}}$ is the vector unknown of the density $\rho\in\mathbb{R}^+$, of the momentum density vector $\boldsymbol{m} = (m_x, m_y, m_\theta)^{\mathrm{T}} \in \mathbb{R}^3$, with x, y and θ axial, radial and angular coordinates of a cylindrical coordinate system, respectively, and of the total (internal plus kinetic) energy per unit volume E^{t} and where

$$\mathbf{f}(\mathsf{u}) = \left(\boldsymbol{m}, \frac{\boldsymbol{m}\otimes\boldsymbol{m}}{\rho} + \Pi(\mathsf{u})\boldsymbol{I}, \frac{\boldsymbol{m}}{\rho}(E^{\mathrm{t}} + \Pi(\mathsf{u}))\right)^{\mathrm{T}} \in \mathbb{R}^5\times\mathbb{R}^3 \tag{B.2}$$

with $\Pi = \Pi(\mathsf{u})$ the pressure as a function of the conservative variables. In cylindrical coordinates, the flux vector reads

$$\mathbf{f}(\mathsf{u}) = \begin{pmatrix} m_x\hat{\boldsymbol{x}} + m_y\hat{\boldsymbol{y}} + m_\theta\hat{\boldsymbol{\theta}} \\ \left[\frac{m_x^2}{\rho} + \Pi(\mathsf{u})\right]\hat{\boldsymbol{x}} + \frac{m_x m_y}{\rho}\hat{\boldsymbol{y}} + \frac{m_x m_\theta}{\rho}\hat{\boldsymbol{\theta}} \\ \frac{m_x m_y}{\rho}\hat{\boldsymbol{x}} + \left[\frac{m_y^2}{\rho} + \Pi(\mathsf{u})\right]\hat{\boldsymbol{y}} + \frac{m_y m_\theta}{\rho}\hat{\boldsymbol{\theta}} \\ \frac{m_x m_\theta}{\rho}\hat{\boldsymbol{x}} + \frac{m_y m_\theta}{\rho}\hat{\boldsymbol{y}} + \left[\frac{m_\theta^2}{\rho} + \Pi(\mathsf{u})\right]\hat{\boldsymbol{\theta}} \\ \frac{m_x}{\rho}H^{\mathrm{t}}(\mathsf{u})\hat{\boldsymbol{x}} + \frac{m_y}{\rho}H^{\mathrm{t}}(\mathsf{u})\hat{\boldsymbol{y}} + \frac{m_\theta}{\rho}H^{\mathrm{t}}(\mathsf{u})\hat{\boldsymbol{\theta}} \end{pmatrix} \begin{matrix} \\ \\ \text{Momentum fluxes} \\ \\ \end{matrix}$$

Mass flux

Energy flux

where the shorthand $H^{\mathrm{t}}(\mathsf{u}) = E^{\mathrm{t}} + \Pi(\mathsf{u})$, total enthalpy per unit volume, has been used and where $\hat{\boldsymbol{x}}, \hat{\boldsymbol{y}}$ and $\hat{\boldsymbol{\theta}}$ are the axial, radial and angular coordinate unit vectors, respectively. Note that $\hat{\boldsymbol{y}} = \hat{\boldsymbol{y}}(\theta)$ and $\hat{\boldsymbol{\theta}} = \hat{\boldsymbol{\theta}}(\theta)$. The expression above shows the flux function as a vector of five components; the first one is associated with the mass conservation law, the second, the third and the fourth ones stem from the momentum conservation law and the last one pertains to the energy conservation law. Each component of $\mathbf{f}(\mathsf{u})$ is in fact a vector in the three-dimensional space Ω, with components in $(\hat{\boldsymbol{x}}, \hat{\boldsymbol{y}}, \hat{\boldsymbol{\theta}})^{\mathrm{T}}$. Note that the above vector representation of the flux function is not the standard matrix form used for example in [48].

By recalling the expression for the divergence operator in cylindrical coordinates, namely,

$$\nabla\cdot\boldsymbol{q} = \frac{\partial q_x}{\partial x} + \frac{1}{y}\frac{\partial}{\partial y}[yq_y] + \frac{1}{y}\frac{\partial q_\theta}{\partial\theta}$$

where q_x, q_y and q_θ are the axial, radial and angular components of the vector $\boldsymbol{q} \in \mathbb{R}^3$, respectively, and by recalling that $\partial\hat{\boldsymbol{y}}/\partial\theta = \hat{\boldsymbol{\theta}}$ and $\partial\hat{\boldsymbol{\theta}}/\partial\theta = -\hat{\boldsymbol{y}}$, one immediately obtains the divergence of the vector of the momentum fluxes as

$$\begin{aligned}\nabla\cdot\left[\frac{\boldsymbol{m}\otimes\boldsymbol{m}}{\rho}+\Pi(\mathsf{u})\boldsymbol{I}\right] &= \hat{\boldsymbol{x}}\frac{\partial}{\partial x}\left[\frac{m_x^2}{\rho}+\Pi(\mathsf{u})\right]+\hat{\boldsymbol{y}}\frac{\partial}{\partial x}\left(\frac{m_x m_y}{\rho}\right)+\hat{\boldsymbol{\theta}}\frac{\partial}{\partial x}\left(\frac{m_x m_\theta}{\rho}\right)\\ &+\frac{1}{y}\left\{\hat{\boldsymbol{x}}\frac{\partial}{\partial y}\left(y\frac{m_x m_y}{\rho}\right)+\hat{\boldsymbol{y}}\frac{\partial}{\partial y}\left[y\left(\frac{m_y^2}{\rho}+\Pi(\mathsf{u})\right)\right]+\hat{\boldsymbol{\theta}}\frac{\partial}{\partial y}\left(y\frac{m_x m_\theta}{\rho}\right)\right\}\\ &+\frac{1}{y}\left\{-\hat{\boldsymbol{y}}\left[\frac{m_\theta^2}{\rho}+\Pi(\mathsf{u})\right]+\hat{\boldsymbol{\theta}}\frac{m_y m_\theta}{\rho}\right\},\end{aligned}$$

where the condition of axial symmetry, namely, $\partial\mathsf{u}/\partial\theta \equiv 0$ has been enforced. By multiplying each equation by y, the final form of the Euler equations for axisymmetric problems finally reads

$$\begin{cases}\dfrac{\partial[y\rho]}{\partial t}+\dfrac{\partial[ym_x]}{\partial x}+\dfrac{\partial[ym_y]}{\partial y}=0,\\ \dfrac{\partial[ym_x]}{\partial t}+\dfrac{\partial}{\partial x}\left[y\left(\dfrac{m_x^2}{\rho}+\Pi(\mathsf{u})\right)\right]+\dfrac{\partial}{\partial y}\left[y\dfrac{m_x m_y}{\rho}\right]=0,\\ \dfrac{\partial[ym_y]}{\partial t}+\dfrac{\partial}{\partial x}\left[y\dfrac{m_x m_y}{\rho}\right]+\dfrac{\partial}{\partial y}\left[y\left(\dfrac{m_y^2}{\rho}+\Pi(\mathsf{u})\right)\right]=\dfrac{m_\theta^2}{\rho}+\Pi(\mathsf{u}),\\ \dfrac{\partial[ym_\theta]}{\partial t}+\dfrac{\partial}{\partial x}\left[y\dfrac{m_x m_\theta}{\rho}\right]+\dfrac{\partial}{\partial y}\left[y\dfrac{m_y m_\theta}{\rho}\right]=-\dfrac{m_y m_\theta}{\rho},\\ \dfrac{\partial[yE^{\mathrm{t}}]}{\partial t}+\dfrac{\partial}{\partial x}\left[y\dfrac{m_x}{\rho}(E^{\mathrm{t}}+\Pi(\mathsf{u}))\right]+\dfrac{\partial}{\partial y}\left[y\dfrac{m_y}{\rho}(E^{\mathrm{t}}+\Pi(\mathsf{u}))\right]=0,\end{cases}$$

or, resorting to a vector notation

$$\frac{\partial[y\mathsf{u}]}{\partial t}+\nabla\cdot[y\mathbf{f}(\mathsf{u})]=\mathsf{s}(\mathsf{u}), \tag{B.3}$$

where now $\nabla\cdot(\boldsymbol{r}) = \partial r_x/\partial x + \partial r_y/\partial y$, with $\boldsymbol{r} = (r_x, r_y)^{\mathrm{T}} \in \mathbb{R}^2$, and where

$$\mathbf{f}(\mathsf{u}) = \left(\boldsymbol{m}, \frac{\boldsymbol{m}\otimes\boldsymbol{m}}{\rho}+\Pi(\mathsf{u})\boldsymbol{I}, \frac{\boldsymbol{m}}{\rho}m_\theta, \frac{\boldsymbol{m}}{\rho}(E^{\mathrm{t}}+\Pi(\mathsf{u}))\right)^{\mathrm{T}} \in \mathbb{R}^5\times\mathbb{R}^2 \tag{B.4}$$

with $\boldsymbol{m} = (m_x, m_y)^{\mathrm{T}} \in \mathbb{R}^2$ and $\boldsymbol{I}$ identity matrix of order two. Note that the angular component of the momentum density has been lifted from the momentum vector $\boldsymbol{m}$ and "downgraded" to the rôle of an advected scalar quantity, but for its contributions to the source vector, that reads

$$\mathsf{s}(\mathsf{u}) = \left(0, 0, \frac{m_\theta^2}{\rho}+\Pi(\mathsf{u}), -\frac{m_y m_\theta}{\rho}, 0\right)^{\mathrm{T}} \in \mathbb{R}^5. \tag{B.5}$$

System (B.3) for axisymmetric compressible swirling flows is found to be formally coincident with the Euler equation (19) for axisymmetric flows with no swirl considered in the preceding sections. Therefore, the proposed numerical scheme can be easily applied also to the computation of swirling flows. To this purpose, an additional equation, namely, the conservation of the angular component of the momentum m_θ, is to be added to (19) and the source vector is to be modified according to definition (B.5), see definition (21) for comparison. The discrete representation of the new equation, which is very similar to the mass conservation one, does not require any special treatment and/or the introduction of new metric quantities with respect to those already considered. The modification of the whole procedure is therefore straightforward.

To conclude, we notice in passing that the Roe linearization problem (27) is to be extended to include the new (transport) equation for m_θ. An easy computation shows that the Roe intermediate state is left unchanged, but for the inclusion of an additional intermediate angular velocity, and that the eigenvalues of

the Roe matrix for swirling flows are coincident with the previous one, where now the multiplicity of the eigenvalue associated with linearly degenerate fields is three instead of two, a results that points to the purely advective nature of the additional equation expressing the conservation of the angular component m_θ of the momentum density.

References

[1] A. Dervieux, Steady Euler simulation using unstructured meshes, in: Geymonat (Ed.), Partial Differential Equations of Hyperbolic Type and Applications, World Scientific, Singapore, 1987, pp. 34–105.
[2] T.J. Barth, Aspects of unstructured grids and finite-volume solvers for the Euler and Navier–Stokes equations, AGARD AR 787-6 on unstructured grid methods for advection dominated flows, NATO, 1992.
[3] V. Selmin, The node-centred finite volume approach: bridge between finite differences and finite elements, Comput. Methods Appl. Mech. Eng. 102 (1993) 107–138.
[4] P. Rostand, B. Stoufflet, TVD schemes to compute compressible viscous flows on unstructured grids, in: J. Ballmann, R. Jeltsch (Eds.), Nonlinear Hyperbolic Equations – Theory, Computation Methods, and Applications, Vieweg, Braunschweig, 1989.
[5] P. Arminjon, A. Madrane, A mixed finite volume/finite element method for 2-dimensional compressible Navier–Stokes equations on unstructured grids, in: M. Fey, R. Jeltsch (Eds.), Hyperbolic Problems – Theory, Numerics, Applications, International Series of Numerical Mathematics, vol. 129, Birkhäuser, Basel, 1998.
[6] C. Debiez, A. Dervieux, K. Mer, B. Nkonga, Computation of unsteady flows with mixed finite volume/finite element upwind methods, Int. J. Numer. Meth. Fluids 27 (1998) 193–206.
[7] C. Debiez, A. Dervieux, Mixed-element-volume MUSCL methods with weak viscosity for steady and unsteady flow calculations, Comput. Fluids 29 (2000) 89–118.
[8] V. Selmin, L. Formaggia, Unified construction of finite element and finite volume discretizations for compressible flows, Int. J. Numer. Meth. Eng. 39 (1996) 1–32.
[9] A. Jameson, W. Schmidt, E. Turkel, Numerical solutions of the Euler equations by finite volume methods using Runge–Kutta time stepping schemes, in: AIAA 14th Fluid and Plasma Dynamic Conference, 1981, pp. 1–17, AIAA Paper 81-1259.
[10] B. van Leer, Towards the ultimate conservative difference scheme II. Monotonicity and conservation combined in a second order scheme, J. Comput. Phys. 14 (1974) 361–370.
[11] P.L. Roe, Approximate Riemann solvers, parameter vectors, and difference schemes, J. Comput. Phys. 43 (1981) 357–372.
[12] P.K. Sweby, High resolution schemes using flux limiters for hyperbolic conservation laws, SIAM J. Numer. Anal. 21 (1984) 985–1011.
[13] R. Cummings, H. Yang, Y. Oh, Supersonic, turbulent flow computation and drag optimization for axisymmetric afterbodies, Comput. Fluids 24 (1995) 487–507.
[14] C. Tam, Advances in numerical boundary conditions for computational aeroacoustics, AIAA Paper AIAA-97-1774, 1997.
[15] W. Wood, W. Kleb, 2D/axisymetric formulation of multi-dimensional upwind scheme, in: 15th AIAA Computational Fluid Dynamics Conference, 2001, AIAA-2001-2630.
[16] E. Godlewski, P.A. Raviart, Numerical Approximation of Hyperbolic Systems of Conservation Laws, Springer, New York, 1994.
[17] A. Goudjo, J.-A. Desideri, Un schema de volumes-finis décentré pour la résolution des équations d'Euler en axisymmétrique, Report 1005, INRIA, 1989.
[18] A. Quarteroni, A. Valli, Numerical Approximation of Partial Differential Equations, Springer Series in Computational Mathematics, vol. 23, Springer, Berlin, 1994.
[19] A. Kufner, Weighted Sobolev spaces, Teubner Verlagsgesellschafti, Teubner-Texte zur Mathematik, Band 31, Teubner, Stuttgar, 1980, also published by John Wiley & Sons, 1985.
[20] C. Bernardi, M. Dauge, Y. Maday, Spectral Methods for Axisymmetric Domains, Gauthier-Villars, Paris, 1999.
[21] J. Donea, A. Huerta, Finite Element Methods for Flow Problems, Wiley, New York, 2002.
[22] A. Ern, J.L. Guermond, Theory and Practice of Finite Elements, Applied Mathematical Science, vol. 159, Springer, New York, 2004.
[23] A. Guardone, L. Quartapelle, Spatially factorized Galerkin and Taylor–Galerkin schemes for multidimensional conservation laws, Scientific Report DIA-SR 00-18, Politecnico di Milano, Italy, 2000.
[24] R.J. LeVeque, Finite Volume Methods for Conservation Laws and Hyperbolic Systems, Cambridge University Press, Cambridge, 2002.
[25] L. Galgani, A. Scotti, On subadditivity and convexity properties of thermodynamic functions, Pure Appl. Chem. 22 (1970) 229–235.
[26] H.B. Callen, Thermodynamics and An Introduction to Thermostatistics, second ed., Wiley, New York, 1985.
[27] L. Mottura, L. Vigevano, M. Zaccanti, An evaluation of Roe's scheme generalizations for equilibrium real gas flows, J. Comput. Phys. 138 (1997) 354–399.
[28] A. Guardone, L. Vigevano, Roe linearization for the van der Waals gas, J. Comput. Phys. 175 (2002) 50–78.
[29] N. Weatherill, O. Hassan, M. Marchant, D. Marcum, Adaptive inviscid solutions for aerospace geometries on efficiently generated unstructured tetrahedral meshes, AIAA Paper 93-3390, 1993.
[30] R. Löhner, Applied CFD Techniques, Wiley, New York, 2001.
[31] G. Strang, On the construction and comparison of difference schemes, SIAM J. Numer. Anal. 5 (1968) 506–517.
[32] C.-W. Shu, Total-variation-diminishing time discretizations, SIAM J. Sci. Stat. Comput. 9 (6) (1988) 1073–1084.
[33] M.B. Giles, Stability analysis of a Galerkin/Runge–Kutta Navier–Stokes discretization on unstructured tetrahedral grids, J. Comput. Phys. 132 (1997) 201–214.

[34] T.A. Davis, I.S. Duff, A combined unifrontal/multifrontal method for unsymmetric sparse matrices, ACM Trans. Math. Software 25 (1) (1999) 1–19.
[35] P. Lax, B. Wendroff, System of conservation laws, Commun. Pure Appl. Math. 13 (1960) 217–237.
[36] J. Donea, A Taylor–Galerkin method for convective transport problems, Int. J. Numer. Meth. Eng. 20 (1984) 101–119.
[37] C.-W. Shu, S. Osher, Efficient implementation of essentially non-oscillatory shock-capturing schemes, J. Comput. Phys. 77 (1988) 439–471.
[38] X.-D. Liu, S. Osher, T. Chan, Weighted essentially non-oscillatory schemes, J. Comput. Phys. 115 (1994) 200–212.
[39] M.A. Nettleton, Shock attenuation in a 'gradual' area expansion, J. Fluid Mech. 60 (1973) 209–223.
[40] E.M. Rothkopf, W. Low, Diaphragm opening process in shock tubes, Phys. Fluids 17 (6) (1974) 1169–1173.
[41] R.S. Hickman, L.C. Farrar, J.B. Kyser, Behavior of burst diaphragms in shock tubes, Phys. Fluids 18 (10) (1975) 1249–1252.
[42] P. Petrie-Repar, P.A. Jacobs, A computational study of shock speeds in high-performance shock tubes, Shock Waves 8 (1998) 79–91.
[43] G. Persico, P. Gaetani, A. Guardone, Dynamic calibration of fast-response probes in low-pressure shock tubes, Meas. Sci. Technol. 16 (2005) 1751–1759.
[44] M. Sun, K. Takayama, Vorticity production in shock diffraction, J. Fluid Mech. 478 (2003) 237–256.
[45] H. Katanoda, Y. Miyazato, M. Masuda, K. Matsuo, Pitot pressure of correctly-expanded and underexpanded free jets from axisymmetric supersonic nozzles, Shock Waves 10 (2) (2000) 95–101.
[46] M. Abbet, Mach disk in underexpanded exhaust plumes, AIAA J. 9 (3) (1971) 512–514.
[47] A.L. Addy, Effect of axisymmetric sonic nozzle geometry on Mach disk characteristics, AIAA J. 19 (1) (1981) 121–122.
[48] M. Vinokur, J.L. Montagné, Generalized flux-vector splitting and Roe average for an equilibrium real gas, J. Comput. Phys. 89 (1990) 276.